




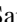















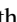


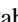


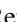












Earliest Galaxies in the JADES Origins Field: Luminosity Function and Cosmic Star Formation Rate Density 300 Myr after the Big Bang

Brant Robertson¹ , Benjamin D. Johnson² , Sandro Tacchella^{3,4} , Daniel J. Eisenstein² , Kevin Hainline⁵ ,
Santiago Arribas⁶ , William M. Baker^{3,4} , Andrew J. Bunker⁷ , Stefano Carniani⁸ , Phillip A. Cargile² ,
Courtney Carreira¹ , Stephane Charlot⁹ , Jacopo Chevallard⁷ , Mirko Curti¹⁰ , Emma Curtis-Lake¹¹ ,
Francesco D'Eugenio^{3,4} , Eiichi Egami⁵ , Ryan Hausen¹² , Jakob M. Helton⁵ , Peter Jakobsen^{13,14} , Zhiyuan Ji⁵ ,
Gareth C. Jones⁷ , Roberto Maiolino^{3,4,15} , Michael V. Maseda¹⁶ , Erica Nelson¹⁷ , Pablo G. Pérez-González⁶ ,
Dávid Puskás^{3,4} , Marcia Rieke⁵ , Renske Smit¹⁸ , Fengwu Sun⁵ , Hannah Übler^{3,4} , Lily Whitler⁵ ,
Christina C. Williams¹⁹ , Christopher N. A. Willmer⁵ , Chris Willott²⁰ , and Joris Witstok^{3,4} 

¹ Department of Astronomy and Astrophysics, University of California, Santa Cruz, 1156 High Street, Santa Cruz, CA 96054, USA

² Center for Astrophysics | Harvard & Smithsonian, 60 Garden Street, Cambridge, MA 02138, USA

³ Kavli Institute for Cosmology, University of Cambridge, Madingley Road, Cambridge, CB3 0HA, UK

⁴ Cavendish Laboratory, University of Cambridge, 19 JJ Thomson Avenue, Cambridge, CB3 0HE, UK

⁵ Steward Observatory, University of Arizona, 933 N. Cherry Avenue, Tucson, AZ 85721, USA

⁶ Centro de Astrobiología (CAB), CSICINTA, Cra. de Ajalvir Km. 4, 28850- Torrejón de Ardoz, Madrid, Spain

⁷ Department of Physics, University of Oxford, Denys Wilkinson Building, Keble Road, Oxford, OX1 3RH, UK

⁸ Scuola Normale Superiore, Piazza dei Cavalieri 7, I-56126 Pisa, Italy

⁹ Sorbonne Université, CNRS, UMR 7095, Institut d'Astrophysique de Paris, 98 bis bd Arago, 75014 Paris, France

¹⁰ European Southern Observatory, Karl-Schwarzschild-Strasse 2, 85748 Garching, Germany

¹¹ Centre for Astrophysics Research, Department of Physics, Astronomy and Mathematics, University of Hertfordshire, Hatfield, AL10 9AB, UK

¹² Department of Physics and Astronomy, The Johns Hopkins University, 3400 N. Charles Street, Baltimore, MD 21218, USA

¹³ Cosmic Dawn Center (DAWN), Copenhagen, Denmark

¹⁴ Niels Bohr Institute, University of Copenhagen, Jagtvej 128, DK-2200, Copenhagen, Denmark

¹⁵ Department of Physics and Astronomy, University College London, Gower Street, London, WC1E 6BT, UK

¹⁶ Department of Astronomy, University of Wisconsin-Madison, 475 N. Charter Street, Madison, WI 53706, USA

¹⁷ Department for Astrophysical and Planetary Science, University of Colorado, Boulder, CO 80309, USA

¹⁸ Astrophysics Research Institute, Liverpool John Moores University, 146 Brownlow Hill, Liverpool L3 5RF, UK

¹⁹ NSF's National Optical-Infrared Astronomy Research Laboratory, 950 North Cherry Avenue, Tucson, AZ 85719, USA

²⁰ NRC Herzberg, 5071 West Saanich Road, Victoria, BC V9E 2E7, Canada

Received 2023 December 14; revised 2024 April 28; accepted 2024 April 30; published 2024 July 12

Abstract

We characterize the earliest galaxy population in the JADES Origins Field, the deepest imaging field observed with JWST. We make use of ancillary Hubble Space Telescope optical images (five filters spanning 0.4–0.9 μm) and novel JWST images with 14 filters spanning 0.8–5 μm , including seven medium-band filters, and reaching total exposure times of up to 46 hr per filter. We combine all our data at $>2.3 \mu\text{m}$ to construct an ultra-deep image, reaching as deep as ≈ 31.4 AB mag in the stack and 30.3–31.0 AB mag (5σ , $r=0''.1$ circular aperture) in individual filters. We measure photometric redshifts and use robust selection criteria to identify a sample of eight galaxy candidates at redshifts $z = 11.5$ –15. These objects show compact half-light radii of $R_{1/2} \sim 50$ –200 pc, stellar masses of $M_* \sim 10^7$ – $10^8 M_\odot$, and star formation rates ~ 0.1 – $1 M_\odot \text{ yr}^{-1}$. Our search finds no candidates at $15 < z < 20$, placing upper limits at these redshifts. We develop a forward-modeling approach to infer the properties of the evolving luminosity function without binning in redshift or luminosity that marginalizes over the photometric redshift uncertainty of our candidate galaxies and incorporates the impact of nondetections. We find a $z = 12$ luminosity function in good agreement with prior results, and that the luminosity function normalization and UV luminosity density decline by a factor of ~ 2.5 from $z = 12$ to $z = 14$. We discuss the possible implications of our results in the context of theoretical models for evolution of the dark matter halo mass function.

Unified Astronomy Thesaurus concepts: [Early universe \(435\)](#); [Galaxy formation \(595\)](#); [Galaxy evolution \(594\)](#); [High-redshift galaxies \(734\)](#); [Reionization \(1383\)](#)

1. Introduction

JWST has pushed the forefront of our knowledge of galaxies in the distant Universe to the first 350 million years of cosmic time. Within the first weeks of operations, surveys with JWST unveiled galaxy candidates beyond redshift $z \sim 12$ in an epoch when only the most optimistic models of the cosmic star formation rate

(SFR) density predicted that galaxies would be easily discoverable (Naidu et al. 2022a; Castellano et al. 2022; Adams 2023; Donnan et al. 2023b; Harikane et al. 2023; Atek et al. 2023; Bouwens et al. 2023; Morishita & Stiavelli 2023; Finkelstein et al. 2024). The identification and spectroscopic confirmation by the JWST Advanced Deep Extragalactic Survey (JADES; Pis: Rieke and Lutzgendorf; Eisenstein et al. 2023a) of the galaxies JADES-GS-z12-0 at $z = 12.6$ and JADES-GS-z13-0 at $z = 13.2$ affirmatively established for the first time the reality of galaxies at $z > 12$ (Curtis-Lake et al. 2023; D'Eugenio et al. 2023; Robertson et al. 2023). Subsequently, other galaxy candidates have been

confirmed at $z \sim 12\text{--}13$ in other surveys (Wang et al. 2023; Fujimoto et al. 2023) and many additional high-redshift candidates identified photometrically (e.g., Pérez-González et al. 2023a; Leung et al. 2023; Hainline et al. 2024b).

The discovery of these distant sources raises substantial questions about the nature of galaxy formation in the early Universe (Shen et al. 2023a; Dekel et al. 2023; Ferrara et al. 2023; Li et al. 2023; Lovell et al. 2023; Mason et al. 2023; Yung et al. 2024). The earliest known galaxies appear relatively bright (e.g., Naidu et al. 2022a; Castellano et al. 2022; Finkelstein et al. 2023; Treu et al. 2023), show a range of stellar masses $M_* \sim 10^7\text{--}10^9 M_\odot$, and have young stellar ages of $t_* \sim 10^7\text{--}10^8$ yr (Robertson et al. 2023). Structurally, these galaxies show physical sizes of $r \sim 0.1\text{--}1$ kpc and SFR surface densities of $\dot{\Sigma}_* \sim 50\text{--}100 M_\odot \text{ yr}^{-1} \text{ kpc}^{-2}$ (Wang et al. 2023; Arrabal Haro et al. 2023; Robertson et al. 2023). They are compact star-forming galaxies undergoing rapid star formation on a timescale comparable to their local dynamical times. Individually, the properties of these objects are not extreme given the densities and dynamics of the early Universe. Collectively, the apparent, albeit uncertain, abundance of such objects in the context of structure formation may be unexpectedly high. Resolving this essential quandary requires statistical constraints on the abundance of $z > 12$ galaxies and information on their possible origins through higher-redshift searches.

To answer these questions, this work presents first results on the search for distant galaxies in the JADES Origins Field (JOF; Program ID 3215, PIs: Eisenstein and Maiolino; Eisenstein et al. 2023b). The JOF observations were designed to use JWST medium bands, including NIRCcam F162M, to isolate the Ly α break at $z \gtrsim 12$ and simultaneously control for contamination by lower-redshift line emitters that can mimic the broadband spectral energy distributions (SEDs) of distant galaxies (Naidu et al. 2022b; Pérez-González et al. 2023b; Arrabal Haro et al. 2023; Zavala et al. 2023). In concert with ultradeep broadband observations from JADES, the 9.05 arcmin² JOF provides the best current data set for finding and characterizing $z \gtrsim 12$ galaxies. We search the JOF for objects to an effective limiting depth of $f_\nu \sim 2\text{--}3$ nJy, performing SED-fitting analyses to select the highest-redshift candidates. We then use a forward-modeling approach to infer the characteristics of the evolving luminosity function given the properties of our sample of high-redshift candidate galaxies. Our method accounts for the photometric redshift posterior constraints of our sample’s galaxies without binning in redshift or luminosity. We employ our method to study the behavior of the evolving luminosity function beyond $z \sim 12$ and the abundance of galaxies at earlier times.

This paper is organized as follows. In Section 2 we review the JOF data, the observations, data reduction procedure, source detection, and photometry. In Section 3, we describe our selection procedure based on SED template fitting. Forward-modeling constraints on the galaxy candidate structural properties and inference of the distant stellar population properties are described in Section 4. We characterize the galaxy luminosity functions at $z \sim 12\text{--}15$ and our constraints on the UV luminosity density at $z \sim 12\text{--}20$ in Section 5, and report the inferred physical properties of the high-redshift candidates in Section 6. We interpret the observational results in the context of galaxy formation theory in Section 7. We summarize our conclusions and preview future work in Section 8. Throughout

this work, we use the AB magnitude system (Oke & Gunn 1983) and assume a flat Lambda cold dark matter (Λ CDM) cosmology with $\Omega_m = 0.3$ and $H_0 = 70 \text{ km s}^{-1} \text{ Mpc}^{-1}$.

2. Data

This work uses JWST observations in the JOF to discover and constrain the abundance and properties of $z > 12$ galaxies. In Section 2.1 we review the JOF and accompanying JADES and Hubble Space Telescope (HST) observations. In Section 2.2, we present the data reduction methods used to process the imagery. The detection and photometric methods used to discover the objects are described in Section 2.3.

2.1. Observations

Eisenstein et al. (2023b) presents the JOF, a single JWST/NIRCcam pointing of exceptional depth, with about 7 days of exposure time spread between 14 filters covering an $A \sim 9$ arcmin² area. The JOF began with the parallel imaging of deep JADES spectroscopy (Program ID 1210, presented in Bunker et al. 2023) that produced long F090W, F115W, F150W, F200W, F277W, F335M, F356W, F410M, and F444W exposures in a field adjacent to the Hubble Ultra Deep Field (UDF) within the Great Observatories Origins Deep Survey South (GOODS-S) field. This campaign continued in Cycle 2 Program ID 3215, which observed in six JWST/NIRCcam medium bands—F162M, F182M, F210M, F250M, F300M, and F335M—again acquired in parallel to deep NIRSpec observations. We also include all JADES GOODS-S medium-depth imaging (Program ID 1180) that overlaps with the JOF. This area of GOODS-S partially overlaps with the FRESCO (Program ID 1895) F182M, F210M, and F444W data, which we incorporate. The field also has partial coverage of HST Advanced Camera for Surveys (ACS) F435W, F606W, F775W, F814W and F850LP images reduced and released through the Hubble Legacy Field program (Illingworth et al. 2016) as well as reductions of GOODS (Giavalisco et al. 2004) and Cosmic Assembly Near-infrared Deep Extragalactic Legacy Survey (CANDELS; Grogin et al. 2011; Koekemoer et al. 2011) images. In total, these data provide 19 JWST and HST photometric bands that we use to constrain the galaxy SEDs and particularly the Ly α break.

2.2. Data Reduction

Our image reduction methods were outlined in Rieke et al. (2023) and Eisenstein et al. (2023a), detailed in S. Tacchella et al. (2024, in preparation), and we provide a summary here. We process the images with the `jwst` Calibration Pipeline (version 1.11.4) and Calibration Reference Data System pipeline mapping 1130, which includes in-flight NIRCcam dark, distortion, bad pixel mask, read noise, superbias and flat reference files.

We use `jwst` Stage 1 to perform the detector-level corrections and ramp fitting. We run this stage with the default parameters, except for the correction of “snowball” artifacts from cosmic rays. The identification and correction of snowballs represent a big challenge. Heuristically, we find that the following parameters provide reasonable snowball amelioration: `max_jump_to_flag_neighbors = 1`, `min_jump_to_flag_neighbors = 100,000`, `min_jump_area = 5`, `min_sat_area = 1`, `expand_factor = 2`, `min_sat_radius_extend = 2.5`, and `max_extended_radius = 200`.

As detailed in Rieke et al. (2023), we run `jwst` Stage 2 with the default parameters, but replace the STScI flats for all long-

wavelength (LW) bands except F250M and F300M with custom supersky flats. When we do not have sufficient images to produce a robust flat-field, we interpolated the flat-field images from the bands adjacent in wavelength. Following Stage 2, we perform custom corrections for all additive effects including $1/f$ noise, scattered light effects (“wisps” and “claws”), and the large-scale background. Furthermore, we also updated the DQ data quality array to mask additional features imprinted visually onto the mosaics, including persistence, uncorrected wisp features, and unflagged hot pixels.

Before running `jwst` Stage 3, we perform astrometric registration to Gaia DR2 (G. Brammer private communication; Gaia Collaboration et al. 2018) with a modified `jwst` pipeline `tweakreg` code. We apply both a rotation and offset to the individual level-2 images. For images taken in the A module with the medium bands F182M, F210M, and F335M, we replace the default distortion maps with the nearest (in effective wavelength) wide-band distortion map for that detector.

We construct the mosaics using `jwst` Stage 3. We create single mosaics for each filter by combining exposures from all observations, and run `jwst` Stage 3 with the default parameter values while setting the pixel scale to $0''.03 \text{ pixel}^{-1}$ and a drizzle parameter of `pixfrac = 1` for the short-wavelength (SW) and LW images. Finally, we perform a custom background subtraction, following the procedure outlined in Bagley et al. (2023a). For F090W, F115W, and F150W, hot pixels that pass median rejection are replaced with median-filtered values from the local flux image.

2.3. Detection and Photometry

The detection and photometry methods are discussed in Rieke et al. (2023) and Eisenstein et al. (2023a) and will be detailed in B. Robertson et al. (2024, in preparation).

To perform source detection, an inverse variance-weighted stack of the LW NIRCcam F250M, F277W, F300M, F335M, F356W, F410M, and F444W science (SCI) and error (ERR) channels are constructed. Small-scale noise residuals from incomplete masking in the `jwst` pipeline are median filtered from the ERR images. The signal-to-noise ratio (SNR) image created from the ratio of these images is used as the detection image. An initial source significance threshold of $\text{SNR} > 1.5$ is used to select regions of interest, and a series of custom computational morphology algorithms inspired by NoiseChisel (Akhlghi & Ichikawa 2015; Akhlghi 2019) are applied to refine the segmentations. Stars and diffraction spikes are masked by constructing segmentations from stacks of all available filters and integrated into the detection segmentation map. The detection image segmentations are deblended using a logarithmic scaling of the F200W image. High-pass filtering is applied to the outer regions of large segmentations to isolate proximate satellite galaxies. After these refinements of the segmentation map, a final pass to detect potentially missed compact, faint sources is applied. The completeness as a function of flux and size for this detection algorithm has been calculated using source injection simulations and is presented in Section 4.1.

After engineering the segmentation map, we perform a set of customized photometric measurements based on the `photutils` (Bradley et al. 2023) analysis package. Object centroids are computed using the “windowed positions” used by Source Extractor (Bertin & Arnouts 1996). Apertures for measuring Kron (1980) fluxes are determined based on the stacked signal

image (the numerator of the SNR detection image) using a Kron parameter of 2.5. We limit the area of the Kron aperture to be less than twice an object’s segmentation area. In addition to Kron fluxes, we measure circular aperture photometry with aperture radii of $r = \{0''.1, 0''.15, 0''.25, 0''.3, 0''.35, 0''.5\}$. To provide aperture corrections, we produce a model point-spread function (mPSF) following the method of Ji et al. (2023), where we inject WebbPSF models into `jwst` level-2 images and mosaic them using the same exposure pattern as the JOF observations to provide a composite star field. An mPSF for each band (and observing program) is then constructed from these PSF mosaics. The circular aperture corrections are measured and tabulated, and the Kron aperture corrections computed by integrating within the corresponding elliptical apertures are placed on the mPSF. For HST, we measure empirical point-spread functions (ePSFs) using the `photutils` (Bradley et al. 2023) ePSF Builder with visually inspected stars in the field.

We perform a bevy of photometric validation tests. Cross-validation against the CANDELS HST photometry using completely independent HST reductions from the Hubble Legacy Field program are presented in Rieke et al. (2023) for the broader JADES/GOODS-S field. We also compute median photometric offsets from SED templates using EAZY (Brammer et al. 2008), following the method described by Hainline et al. (2024b). We find these zero-point offsets to be within 5.2%, and typically within 1%, for JWST filters.

2.3.1. Surface Brightness Profile Modeling

We also forward model each galaxy’s surface brightness profile using the `Forcepho` code (B. Johnson 2024, in preparation). We use `Forcepho` with custom mPSFs to model the surface brightness profile of each galaxy in our survey simultaneously with any nearby objects in each individual exposure where pixel covariance is minimized. We restrict the modeling to the F200W and F277W bands, to minimize the chance of any PSF mismatch or astrometric errors while maximizing the SNR and resolution. The surface brightness profile is assumed to be a Sérsic (1968) model, with a fast Gaussian-based factorization of the model. `Forcepho` provides a Bayesian estimate of the surface brightness profile parameters, including the galaxy half-light radius. We have used `Forcepho` to study the structure of other extremely high-redshift galaxies (e.g., Robertson et al. 2023; Tacchella et al. 2023), and we refer the reader to Baker et al. (2023) for more details on our morphological analysis methods.

2.4. Image Depths

With the construction of our broad- and medium-band NIRCcam mosaics and the LW ($\lambda > 2.3 \mu\text{m}$) detection image, we can use the photometry method described in Section 2.3 to measure our image depths. In Table 1, we report the median aperture-corrected 5σ point-source depth in each filter and the stack (using the F277W PSF to estimate the stack’s aperture correction). When measuring the depth in each image, we use a dilated version of the segmentation map created by the detection algorithm to mask source pixels. We note that the single-band images depths listed in Table 1 are all within 10%–25% of the 5σ point-source depths we reported in Eisenstein et al. (2023b) that were computed from the JWST exposure time calculator, with the LW filters showing the most improved depth. Our

Table 1
Depths of the JADES Origins Field

Band	Median Depth ^a (nJy)	Median Depth (AB)
JWST/NIRCam Filters		
F090W	2.80	30.28
F115W	2.33	30.48
F150W	2.19	30.55
F162M	2.76	30.30
F182M	1.78	30.77
F200W	2.27	30.51
F210M	2.29	30.50
F250M	2.58	30.37
F277W	1.42	31.02
F300M	1.80	30.76
F335M	1.70	30.82
F356W	1.58	30.90
F410M	2.65	30.34
F444W	2.26	30.52
Stacked Depth at $\lambda > 2.3 \mu\text{m}$		
JOF	0.96	31.44
NGDEEP ^b	0.82	31.61
MIRI-UDF ^c	1.28	31.13
JADES GOODS-S Deep	1.39	31.04

Notes.

^a Median $r = 0''1$ aperture-corrected 5σ point-source depth.

^b This depth reflects our independent processing of the NGDEEP data, and we refer the reader to Bagley et al. (2024) for their depth measurements.

^c This depth reflects our independent processing of the MIRI-UDF data, and we refer the reader to Pérez-González et al. (2023a) for their depth measurements.

single-band images reach 30.3–31.0 AB, and the combined $\lambda > 2.3 \mu\text{m}$ stack reaches 31.4 AB depth. For comparison, we also list the 5σ point-source depth of the corresponding $\lambda > 2.3 \mu\text{m}$ stacks from available NIRCam LW images in NGDEEP (F277W + F356W + F444W; Bagley et al. 2024), the MIRI-UDF NIRCam parallel (F277W + F356W; Pérez-González et al. 2023a), and the JADES GOODS-S Deep region that covers the Hubble UDF (Rieke et al. 2023). To measure their depths, we processed these fields using identical methods and used the same F277W PSF model to aperture correct them. We report depths for each program separately, and note that where the MIRI-UDF parallel and NGDEEP NIRCam imaging overlap the combined depths will be even more sensitive than listed in Table 1.

3. Selection of Redshift $z \gtrsim 12$ Galaxies

The photometric selection of high-redshift galaxies relies on identifying a strong Ly α break in the rest-frame UV of a galaxy’s SED (e.g., Guhathakurta et al. 1990; Steidel et al. 1995). Below, we detail our selection of $z \gtrsim 12$ galaxies based on this feature.

3.1. Photometric Redshift Estimation

To infer the photometric redshifts of galaxies in the JOF, we apply the techniques detailed in Hainline et al. (2024b) to fit templates of galaxy SEDs to our JWST and HST photometry, varying the redshift to assess the relative goodness of fit. To perform the SED fits, we use the EAZY code (Brammer et al. 2008) to compute rapidly the photometric redshift posterior distributions for each galaxy in the JOF survey. When fitting SED templates, we use the template suite described in Hainline

et al. (2024b) that includes models with strong line emission and a range of UV continua. The photometric redshifts estimated from fits to these templates were shown to have an outlier fraction (defined as the fraction of sources with $|z_{\text{phot}} - z_{\text{spec}}| / (1 + z_{\text{spec}}) > 0.15$) of $f_{\text{out}} = 0.05$ in Rieke et al. (2023), and $f_{\text{out}} = 0$ for 42 sources at $z > 8$ in Hainline et al. (2024b). A range of potential redshifts $z = 0.01\text{--}22$ in $\Delta z = 0.01$ increments were considered, and for selection, we adopt the use of the redshift corresponding to the minimum χ^2 from the fit, z_a . For each nominal redshift, we use the Inoue et al. (2014) model for attenuation from the intergalactic medium (IGM; see also Madau 1995). We do not adopt any magnitude priors, we impose an error floor of 5% on the photometry, and allow for negative fluxes. When fitting the SED models to determine a photometric redshift, to maximize the SNR we use aperture-corrected $r = 0''1$ circular aperture fluxes on the native-resolution JOF images without convolution to a common PSF, multiplied by the photometric offsets discussed in Section 2.3. We have checked that we obtain comparably high-redshift solutions when using common PSF Kron aperture photometry with lower SNRs, except where noted below. We note that for some objects, the best-fit SED model has Ly α line emission. This feature arises as an artifact of the optimization process in EAZY that mixes templates with and without Ly α emission. We do not claim this line emission to be real. The equivalent width of Ly α is degenerate with the redshift of the break, which can contribute to a photometric redshift offset of $\Delta z \approx 0.2\text{--}0.4$ relative to a spectroscopic redshift. Local attenuation from the galaxy’s interstellar medium or circumgalactic medium can shift the photometric redshift by a similar amount (e.g., D’Eugenio et al. 2023; Heintz et al. 2024)

3.2. Selection Criteria

In the JOF, we apply the following criteria to identify our high-redshift sample. These criteria have been adapted from Hainline et al. (2024b) but further tailored to a $12 \lesssim z \lesssim 20$ selection. We note that these criteria both select objects previously discovered, notably by Hainline et al. (2024b), and identify new objects. We provide the provenance of each object when discussing our samples below. Our selection criteria are:

1. The redshift at the EAZY fit χ^2 minimum must be $z_a \geq 11.5$.
2. Two of the F277W, F356W, and F444W JWST/NIRCam filters must show $>5\sigma$ detections.
3. All the LW NIRCam fluxes (F250M, F277W, F300M, F335M, F356W, F410M, and F444W) must exceed 1.5 σ significance.
4. The redshift posterior distribution must have an integral probability of $P(z_a > 11) > 0.68$, where we take $P(z) \propto \exp(-\chi^2/2)$.
5. The goodness-of-fit difference between the best high-redshift ($z > 11$) and low-redshift ($z < 7$) solutions must satisfy $\Delta\chi^2 > 4$, and for the best fit we require $\chi^2 < 100$ summed over all 19 filters.
6. The flux in F090W and F115W each must be below 2.5 σ significance, as we expect no robust detection of flux blueward of the Ly α break.
7. To avoid objects redder than the typically blue high-redshift objects (e.g., Topping et al. 2024), we require

Table 2
High-redshift Candidates in the JADES Origins Field

Name	NIRCam ID	R.A.	Decl.	z_{phot}^b	M_{UV}	$R_{1/2}$ [mas] ^b	$P(z < 7)^c$
Main Sample $z > 11.5$							
JADES+53.09731-27.84714	74977	53.09731	-27.84714	$11.53^{+0.27}_{-0.78}$	-17.66 ± 0.14	12^{+8}_{-7}	3.72×10^{-5}
JADES+53.02618-27.88716	16699	53.02618	-27.88716	$11.56^{+0.41}_{-0.46}$	-17.94 ± 0.15	35^{+7}_{-7}	9.12×10^{-4}
JADES+53.04017-27.87603	33309	53.04017	-27.87603	$12.10^{+0.37}_{-0.16}$	-17.73 ± 0.10	12^{+3}_{-3}	4.02×10^{-5}
JADES+53.03547-27.90037	160071	53.03547	-27.90037	$12.38^{+0.17}_{-0.40}$	-18.16 ± 0.11	33^{+4}_{-4}	7.87×10^{-4}
JADES+53.06475-27.89024	13731	53.06475	-27.89024	$12.93^{+0.08}_{-0.16}$	-18.78 ± 0.04	4^{+4}_{-2}	5.12×10^{-24}
JADES+53.02868-27.89301	11457	53.02868	-27.89301	$13.52^{+0.26}_{-0.82}$	-18.55 ± 0.11	19^{+4}_{-4}	7.75×10^{-5}
JADES+53.07557-27.87268	376946	53.07557	-27.87268	$14.38^{+1.05}_{-0.37}$	-18.28 ± 0.22	6^{+6}_{-3}	7.63×10^{-2}
JADES+53.08294-27.85563 ^d	183348	53.08294	-27.85563	$14.39^{+0.23}_{-0.09}$	-21.00 ± 0.05	76^{+2}_{-2}	0
JADES+53.10762-27.86013	55733	53.10762	-27.86013	$14.63^{+0.06}_{-0.75}$	-18.54 ± 0.13	45^{+6}_{-5}	2.26×10^{-2}
Contributing Sample $z < 11.5$							
JADES+53.03139-27.87219	172510	53.03139	-27.87219	$10.76^{+0.66}_{-0.36}$	-17.85 ± 0.10	32^{+8}_{-7}	6.49×10^{-5}
JADES+53.09292-27.84607	76035	53.09292	-27.84607	$11.05^{+0.49}_{-0.42}$	-17.83 ± 0.15	6^{+5}_{-4}	4.06×10^{-4}
JADES+53.06857-27.85093	70836	53.06857	-27.85093	$11.17^{+0.26}_{-0.31}$	-18.02 ± 0.10	5^{+4}_{-3}	2.38×10^{-3}
Auxiliary Sample $z > 11.5$							
JADES+53.08468-27.86666 ^e	44962	53.08468	-27.86666	$12.9^{+1.20}_{-0.25}$	-18.16 ± 0.10	56^{+9}_{-7}	1.09×10^{-2}
JADES+53.07385-27.86072 ^f	54586	53.07385	-27.86072	$13.06^{+0.97}_{-0.49}$	-17.08 ± 0.12	40^{+16}_{-11}	6.16×10^{-2}

Notes.

^a The half-light size refers to the intrinsic, PSF-deconvolved size of each source, in milliarcseconds.

^b Best-fit photometric redshift with 16th and 84th percentile uncertainties from the inferred photometric redshift distribution.

^c The posterior probability density for the photometric redshift of the candidate to lie at redshift $z < 7$, given the SED-fitting method described in Section 3.1.

^d Spectroscopically confirmed at $z = 14.32$ by S. Carniani et al. (2024, in preparation).

^e Fails red color limit.

^f Fails minimum SNR criterion.

that sources cannot have both $(F277W - F356W) > 0.125$ and $(F356W - F444W) > 0.25$.

8. Each object must have F150W, F162M, F182M, F210M, and F277W coverage. This criterion limits our survey area to the F162M JOF footprint.
9. The NIRCam SW and LW local exposure times must be within a factor of 4, which avoids edge effects from the mosaic pattern.
10. To avoid variable sources, the flux in the NIRCam medium bands acquired in the second year of JWST operations must not exceed the broadband NIRCam fluxes acquired in the first year by more than 1σ in all bands simultaneously. In practice, we treat overlapping medium- and broadband filters as random samples of the same flux density, and then flag when the difference between such pairs of flux estimates exceeds the quadrature sum of each pair's errors when taken in different epochs.
11. We require that the source not be covered by another galaxy as determined from the segmentation map, which lowers the available area by 22%. The final available area after accounting for foreground sources is approximately $A' = 7.06 \text{ arcmin}^2$.

We note that without the data quality (criteria 9–10), minimum LW SNR threshold (criteria 2–3), or color criteria (criteria 6–7), 15 objects would be selected. However, of these sources, one (JADES+53.05101-27.89787) sits in an oversubtracted area of a distant star diffraction spike and three more are covered by a stray light “wisp” feature in F162M (JADES+53.08317-27.86572, JADES+53.07681-27.86286, and JADES+53.04964-27.88605). For a discussion of wisp features in JWST, please see Rigby et al. (2023).

Of the remaining 11, one fails the minimum SNR threshold (for JADES+53.07385-27.86072, all filters redward of F335M have $f_\nu < 2 \text{ nJy}$) and one fails the color criteria (JADES+53.08468-27.86666 is red). In total nine objects pass the selection; these comprise our Main Sample (see Table 2). While we will comment on the additional two interesting objects that nearly satisfy our selection, we do not consider them in our fiducial luminosity function analyses. We call this collection of two objects the “Auxiliary Sample” at $z > 11.5$. There are also five sources in the Hainline et al. (2024b) sample in the vicinity of the JOF with previously reported photometric redshifts $z > 11$ that are not in our sample. Of these, with the additional JOF data we find four objects to have revised photometric redshifts $z < 7$ or fail other selection criteria (JADES+53.02700-27.89808, JADES+53.03696-27.89422, JADES+53.07901-27.87154, and JADES+53.10469-27.86187). The fifth falls in the F162M gap (JADES+53.07076-27.86544; NIRCam ID 176151) and therefore does not reside in our effective area.

We note that the F250M SNR criterion fixes the upper redshift limit of our selection. If we remove this criterion and the $z > 11.5$ limit, we find one additional $z \sim 11.4$ candidate (JADES+53.10131-27.85696) detected in all filters F150W and redder with $f_\nu \approx 2 \text{ nJy}$, except F250M, which is about 1.5σ too low. In other words, we would find no $z \gtrsim 20$ candidates by removing the weak F250M detection criterion.

The luminosity function analysis discussed below in Section 5 enables the accounting of potential contributions to the inferred galaxy abundance from galaxies with maximum-likelihood photometric redshifts below the putative redshift of interest. We identified galaxies with maximum-likelihood redshifts $z > 8$ and $P(z > 12) > 0.01$ that otherwise satisfy the above selection criteria. There are three such galaxies, which fall in the photometric redshift $z \approx 10.5\text{--}11.2$ range, which will

Table 3
Aperture-corrected HST/ACS Photometry^a in $r = 0''.1$ Circular Apertures

Name	F435W (nJy)	F606W (nJy)	F775W (nJy)	F814W (nJy)	F850LP (nJy)
Main Sample $z > 11.5$					
JADES+53.09731-27.84714	-1.06 ± 2.49	-0.58 ± 1.35	2.25 ± 3.52	-3.58 ± 1.40	-11.28 ± 4.63
JADES+53.02618-27.88716	-2.47 ± 3.10	-0.79 ± 3.71	-5.52 ± 5.67	2.57 ± 2.33	7.01 ± 7.62
JADES+53.04017-27.87603	0.15 ± 1.70	-1.38 ± 3.37	8.59 ± 5.73	2.04 ± 1.98	-2.17 ± 7.90
JADES+53.03547-27.90037	-3.50 ± 1.73	-2.86 ± 2.40	-2.08 ± 3.28	1.55 ± 2.24	8.51 ± 8.26
JADES+53.06475-27.89024	1.60 ± 2.97	0.47 ± 1.79	-3.36 ± 2.67	4.45 ± 2.30	0.20 ± 5.04
JADES+53.02868-27.89301	-4.05 ± 3.02	-1.82 ± 3.33	4.03 ± 3.64	2.84 ± 2.22	3.77 ± 8.78
JADES+53.07557-27.87268	-0.99 ± 1.88	1.83 ± 1.73	0.99 ± 3.72	0.73 ± 1.80	3.17 ± 4.94
JADES+53.08294-27.85563	-2.80 ± 3.47	0.54 ± 1.36	3.87 ± 3.94	3.67 ± 1.47	1.66 ± 4.45
JADES+53.10762-27.86013	-3.64 ± 2.62	-0.29 ± 1.56	3.47 ± 3.38	-1.35 ± 1.89	-0.35 ± 4.72
Contributing Sample $z < 11.5$					
JADES+53.03139-27.87219	-1.30 ± 1.69	3.82 ± 4.85	-1.02 ± 5.67	-1.37 ± 1.46	5.42 ± 8.00
JADES+53.09292-27.84607	-0.95 ± 2.41	0.69 ± 1.27	0.76 ± 3.56	-2.21 ± 1.41	-2.95 ± 4.35
JADES+53.06857-27.85093	4.54 ± 2.64	2.21 ± 1.33	-7.54 ± 2.83	3.70 ± 1.40	-1.87 ± 3.75
Auxiliary Sample $z > 11.5$					
JADES+53.08468-27.86666	-0.01 ± 2.19	-1.82 ± 1.37	3.51 ± 3.72	-0.03 ± 1.58	-6.87 ± 4.91
JADES+53.07385-27.86072	7.83 ± 2.55	-0.31 ± 1.38	0.98 ± 3.71	-0.17 ± 1.34	0.43 ± 4.35

Note.

^a These photometric measurements were made on the native-resolution Hubble Legacy Field images (Illingworth et al. 2016).

Table 4
Aperture-corrected Short-wavelength JWST/NIRCam Photometry in $r = 0''.1$ Circular Apertures

Name	F090W [nJy]	F115W [nJy]	F150W [nJy]	F162M [nJy]	F182M [nJy]	F200W [nJy]	F210M [nJy]
Main Sample $z > 11.5$							
JADES+53.09731-27.84714	0.67 ± 0.53	-0.01 ± 0.46	2.13 ± 0.46	4.14 ± 0.56	2.93 ± 0.36	3.49 ± 0.52	2.62 ± 0.47
JADES+53.02618-27.88716	0.62 ± 0.61	-0.49 ± 0.50	1.80 ± 0.47	4.10 ± 0.63	3.85 ± 0.45	3.83 ± 0.49	2.83 ± 0.56
JADES+53.04017-27.87603	-0.20 ± 0.59	-0.32 ± 0.49	0.56 ± 0.45	2.81 ± 0.58	3.14 ± 0.42	3.71 ± 0.45	3.43 ± 0.49
JADES+53.03547-27.90037	0.65 ± 0.52	-0.69 ± 0.42	0.65 ± 0.41	2.06 ± 0.53	3.06 ± 0.38	2.49 ± 0.41	2.82 ± 0.48
JADES+53.06475-27.89024	-0.08 ± 0.50	0.29 ± 0.40	0.10 ± 0.37	1.16 ± 0.46	7.80 ± 0.36	6.24 ± 0.42	7.48 ± 0.41
JADES+53.02868-27.89301	-0.82 ± 0.66	0.77 ± 0.54	0.54 ± 0.49	1.46 ± 0.64	4.97 ± 0.46	5.90 ± 0.51	7.46 ± 0.58
JADES+53.07557-27.87268	0.21 ± 0.52	0.21 ± 0.43	-0.82 ± 0.42	0.17 ± 0.52	0.75 ± 0.38	2.18 ± 0.41	0.60 ± 0.46
JADES+53.08294-27.85563	-1.12 ± 0.68	0.73 ± 0.66	1.10 ± 0.55	...	9.73 ± 0.90	20.78 ± 0.58	29.66 ± 1.14
JADES+53.10762-27.86013	0.36 ± 0.56	0.60 ± 0.47	0.16 ± 0.44	0.74 ± 0.61	1.87 ± 0.38	3.37 ± 0.45	3.72 ± 0.53
Contributing Sample $z < 11.5$							
JADES+53.03139-27.87219	-0.41 ± 0.67	0.03 ± 0.56	3.07 ± 0.52	4.70 ± 0.65	4.02 ± 0.47	3.70 ± 0.56	2.95 ± 0.57
JADES+53.09292-27.84607	0.16 ± 0.51	0.26 ± 0.44	2.36 ± 0.50	4.03 ± 0.63	3.43 ± 0.37	3.43 ± 0.54	3.29 ± 0.57
JADES+53.06857-27.85093	0.49 ± 0.48	0.16 ± 0.39	2.36 ± 0.40	3.95 ± 0.49	3.70 ± 0.31	3.56 ± 0.39	3.86 ± 0.43
Auxiliary Sample $z > 11.5$							
JADES+53.08468-27.86666	0.05 ± 0.48	-0.47 ± 0.43	0.38 ± 0.42	0.60 ± 0.46	3.02 ± 0.39	2.78 ± 0.42	3.82 ± 0.44
JADES+53.07385-27.86072	-0.52 ± 0.46	0.26 ± 0.40	0.59 ± 0.38	-0.01 ± 0.48	2.03 ± 0.37	1.55 ± 0.39	1.81 ± 0.44

be referred to as the ‘‘Contributing Sample’’ at $z < 11.5$. Two of these (NIRCam IDs 76035 and 172510) were previously found in Hainline et al. (2024b). A third galaxy, NIRCam ID 64312 with photometric redshift $z \approx 10.6$ and $P(z > 12) \approx 0.05$ from photometry, was subsequently confirmed to lie at slightly lower redshift with $P(z < 12) < 0.01$ and was not considered further.

3.3. Sample

Given the selection criteria presented in Section 3.2, our entire $11.5 < z < 15$ sample consists of eight galaxy candidates (our Main Sample). Table 2 lists their designations based on [R.A., decl.], the internal JADES NIRCam ID, and the best-fit redshift z_a . Five of these objects (IDs 16699, 33309, 13731, 11457, and 55733) were previously identified in Hainline et al. (2024b); the other three are new here. We also record galaxy

sizes measured from our Forcepho modeling in Table 2. For each object, we provide $r = 0''.1$ circular aperture photometry for the HST/ACS bands in Table 3, and JWST $0''.1$ radius circular aperture photometry for the NIRCam SW and LW filters appear in Tables 4 and 5, respectively. Note the fluxes we report in Tables 3–5 are measured on the native-resolution images and are not convolved to a common PSF.

Figure 1 shows an F444W/F200W/F090W red/green/blue false color mosaic of the JOF region. Of the 27.5 arcmin^2 area shown, about 9.05 arcmin^2 has acceptable F162M coverage. The inset thumbnail images for each galaxy candidate show 0.86 arcsec^2 regions with red/green/blue colors provided by F356W + F410M + F444W/F200W + F210M/F090W + F115W, along with the best-fit redshift z_a and the JADES NIRCam ID referenced in Table 2. We plot the

Table 5
Aperture-corrected Long-wavelength JWST/NIRCam Photometry in $r = 0''.1$ Circular Apertures

Name	F250M (nJy)	F277W (nJy)	F300M (nJy)	F335M (nJy)	F356W (nJy)	F410M (nJy)	F444W (nJy)
Main Sample $z > 11.5$							
JADES+53.09731-27.84714	1.68 ± 0.73	2.13 ± 0.33	2.49 ± 0.52	2.25 ± 0.45	2.04 ± 0.35	2.96 ± 0.60	3.07 ± 0.49
JADES+53.02618-27.88716	1.74 ± 0.66	2.15 ± 0.35	2.32 ± 0.46	2.57 ± 0.36	2.17 ± 0.38	1.76 ± 0.63	2.50 ± 0.51
JADES+53.04017-27.87603	2.81 ± 0.75	2.63 ± 0.34	2.70 ± 0.47	2.80 ± 0.37	2.52 ± 0.37	1.71 ± 0.63	1.20 ± 0.51
JADES+53.03547-27.90037	3.16 ± 0.65	3.56 ± 0.34	3.58 ± 0.44	2.73 ± 0.38	2.32 ± 0.39	2.79 ± 0.66	2.47 ± 0.52
JADES+53.06475-27.89024	7.22 ± 0.65	5.34 ± 0.30	5.20 ± 0.46	6.21 ± 0.37	5.47 ± 0.34	5.01 ± 0.58	4.30 ± 0.46
JADES+53.02868-27.89301	5.63 ± 0.69	4.71 ± 0.36	4.55 ± 0.46	3.75 ± 0.37	5.50 ± 0.38	5.79 ± 0.65	5.24 ± 0.51
JADES+53.07557-27.87268	1.80 ± 0.60	2.22 ± 0.33	2.77 ± 0.45	2.27 ± 0.39	2.41 ± 0.35	2.18 ± 0.57	2.20 ± 0.46
JADES+53.08294-27.85563	32.02 ± 0.75	32.83 ± 0.44	31.30 ± 0.55	27.43 ± 0.48	28.21 ± 0.44	28.56 ± 0.71	29.58 ± 0.55
JADES+53.10762-27.86013	3.90 ± 0.70	3.75 ± 0.38	4.25 ± 0.50	4.36 ± 0.45	3.76 ± 0.42	2.68 ± 0.65	4.07 ± 0.49
Contributing Sample $z < 11.5$							
JADES+53.03139-27.87219	2.34 ± 0.69	2.72 ± 0.33	3.51 ± 0.47	2.90 ± 0.38	2.26 ± 0.37	2.21 ± 0.62	3.33 ± 0.51
JADES+53.09292-27.84607	3.96 ± 0.71	2.41 ± 0.34	3.26 ± 0.52	2.51 ± 0.46	2.43 ± 0.37	2.90 ± 0.60	1.69 ± 0.49
JADES+53.06857-27.85093	4.49 ± 0.68	3.63 ± 0.37	3.08 ± 0.49	2.87 ± 0.43	2.98 ± 0.37	3.21 ± 0.59	2.25 ± 0.48
Auxiliary Sample $z > 11.5$							
JADES+53.08468-27.86666	4.31 ± 0.73	4.21 ± 0.36	5.08 ± 0.50	5.14 ± 0.45	4.78 ± 0.39	5.30 ± 0.62	6.14 ± 0.51
JADES+53.07385-27.86072	1.62 ± 0.69	2.12 ± 0.39	2.60 ± 0.51	2.28 ± 0.44	1.84 ± 0.39	1.41 ± 0.64	1.74 ± 0.51

eight galaxy candidates in our Main Sample, and the two auxiliary objects that have photometric redshifts $z > 11.5$ but which fail the data quality or redness cuts.

Next, in order of increasing photometric redshift, we introduce each galaxy candidate with some summary discussion and a figure of the SED fits to the $0''.1$ radius circular aperture photometry. We show the photometric redshift posterior distribution and best-fit redshift for each and the redshift posterior distribution limited to $z < 7$, as well as the best-fit SED and most likely low-redshift SEDs. We also show the JWST filter transmission curves and the 14 JWST filter cutouts for each galaxy.

3.3.1. JADES+53.09731-27.84714; NIRCam ID 74977

Figure 2 shows the best-fit SED for object JADES+53.09731-27.84714 (NIRCam ID 74977). The object is remarkably faint with $m_{AB} \approx 30.5$ redward of Ly α , and has a best-fit redshift of $z_a = 11.5$. The best low-redshift solution has $z_{low} = 2.7$, but exceeds the observed F115W constraint.

3.3.2. JADES+53.02618-27.88716; NIRCam ID 16699

Figure 3 shows the best-fit SED for object JADES+53.02618-27.88716 (NIRCam ID 16699; Hainline et al. 2024b). The best-fit redshift is $z_a = 11.6$ for this faint source, which has $m_{AB} \approx 30.2$ – 30.5 in the NIRCam LW channels. The best low-redshift solution has $z_{low} = 2.6$. We note that using the BAGPIPES SED-fitting code (Carnall et al. 2018) to constrain the photometric redshift of this galaxy candidate provides a slightly lower redshift of $z \approx 11.3$, without Ly α emission and with still nonzero $P(z > 11)$.

3.3.3. JADES+53.04017-27.87603; NIRCam ID 33309

Figure 4 shows the best-fit SED for object JADES+53.04017-27.87603 (NIRCam ID 33309; Hainline et al. 2024b). The best-fit SED model has $z_a = 12.1$, while the best low-redshift solution has $z_{low} = 3.2$. The source is also remarkably faint, with $m_{AB} \approx 30.2$ in the NIRCam LW filters.

3.3.4. JADES+53.03547-27.90037; NIRCam ID 160071

Figure 5 shows the best-fit SED for object JADES+53.03547-27.90037 (NIRCam ID 160071). The flux densities of this object are $f_\nu \approx 3.5$ nJy ($m_{AB} \approx 30$). When fitting an SED model, the observed photometry, including the strong break in F150W, constrain the redshift to be $z_a = 12.4$. The best solution at low redshift has $z_{low} = 3.4$.

3.3.5. JADES+53.06475-27.89024; NIRCam ID 13731

Figure 6 shows the best-fit SED for object JADES+53.06475-27.89024 (NIRCam ID 13731; Hainline et al. 2024b). The LW JWST/NIRCam photometry shows $m_{AB} \approx 29.5$, and constrains the posterior photometric redshift distribution to be peaked strongly near $z_a = 12.9$. The best-fit low-redshift solution at $z_{low} = 3.5$ would exceed the F090W, F115W, F150W, and F162M photometry by several standard deviations.

3.3.6. JADES+53.02868-27.89301; NIRCam ID 11457

Figure 7 shows the best-fit SED for object JADES+53.02868-27.89301 (NIRCam ID 11457; Hainline et al. 2024b). The object has NIRCam flux densities redward of the break of $f_\nu \approx 4$ – 6 nJy ($m_{AB} \approx 29.5$ – 29.9), which constrain the SED models to yield a best-fit redshift $z_a = 13.5$. The best-fit low-redshift solution SED at $z_{low} = 3.6$ exceeds the F090W and F150W constraints by several standard deviations. The second peak in the high-redshift $p(z)$ at $z \approx 12.7$ is driven by the marginal (2.3σ) detection in F162M, which if real would prefer a slightly lower redshift than the mode but still within our selection criteria. However, we caution that the F162M detection, the F182M–F210M color, and the rising SED shape longward of $3.5 \mu\text{m}$ could indicate a potential low-redshift contaminant not well modeled by our SED template set. We therefore proceed with caution while including this candidate in our sample.

3.3.7. JADES+53.07557-27.87268; NIRCam ID 376946

Figure 8 shows the best-fit SED for object JADES+53.07557-27.87268 (NIRCam ID 376946). This faint ($m_{AB} = 30.5$) object at redshift $z_a = 14.4$ is slightly redder than most of the other candidates. JADES+53.07557-27.87268

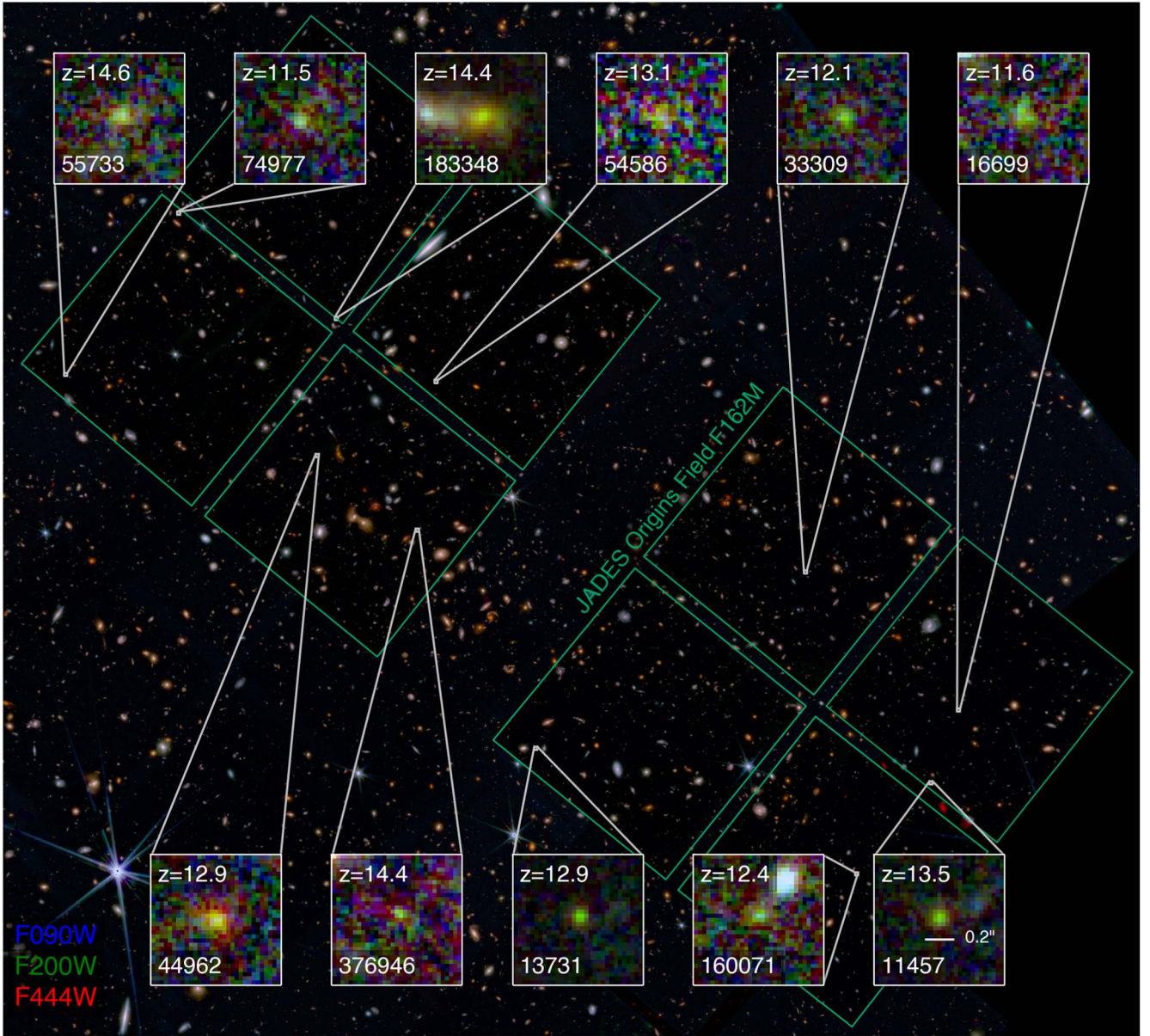


Figure 1. F444W/F200W/F090W false color red/green/blue image of the JOF (background image; 27.5 arcmin^2), the JOF F162M footprint (jade outline) and F356W + F410M + F444W/F200W + F210M/F090W + F115W false color red/green/blue thumbnail images (each 0.86 arcsec^2) for the $z \gtrsim 12$ high-redshift galaxy candidates. The RGB images of the galaxy candidates typically appear to have a green hue in this color space, as they are all detected in the filters used for both the green and red channels, but not the blue channel. Each inset thumbnail lists the best-fit EAZY photometric redshift and the JADES NIRCam ID, and we indicate the shared angular scale of the thumbnails with a scale bar showing $0''.2$. Table 2 lists the designations of the objects based on [R.A., decl.]. NIRCam ID 183348 was spectroscopically confirmed as JADES-GS-z14-0 by S. Carniani et al. (2024, in preparation) at $z = 14.32$.

displays an unusual SED in that the F182M and F210M fluxes must be biased low by several σ to be consistent with the F200W flux, and the high-redshift solution does not match well the observed F182M, F200W, and F210M data. The best solution at low redshift has $z_{\text{low}} = 3.8$ with nearly 8% of the EAZY probability, although it overpredicts the observed F150W flux. We note that when using the BAGPIPES SED-fitting code (Carnall et al. 2018) with a broad log-uniform prior ($M_* \in [10^5, 10^{13}] M_\odot$) on stellar mass to constrain the photometric redshift of this galaxy candidate, we find a yet larger low-redshift probability density than with EAZY. The best-fit redshift is still $z > 14$ and most of its photometric redshift posterior probability is at very high redshift. We also note that this object has the largest increase in the low-redshift probability density when using common PSF Kron aperture

fluxes to fit a photometric redshift, but, given the loss in SNR for this exceedingly faint object, the photometric SED become much noisier.

3.3.8. JADES+53.08294-27.8556; NIRCam ID 183348

JADES+53.08294-27.8556 (NIRCam ID 183348) with redshift $z = 14.4$ is the most remarkable object in our sample, with its best-fit SED shown in Figure 9. The object appears relatively bright ($f_\nu \approx 30 \text{ nJy}$; $r = 0''.1$ radius aperture) but shows strong break from F210M to F182M and no significant flux at shorter wavelengths. Before the JOF ultra-deep JWST/NIRCam medium-band data were acquired, based on JADES JWST/NIRCam broadband data Hainline et al. (2024b) first discussed this source with a photometric redshift of

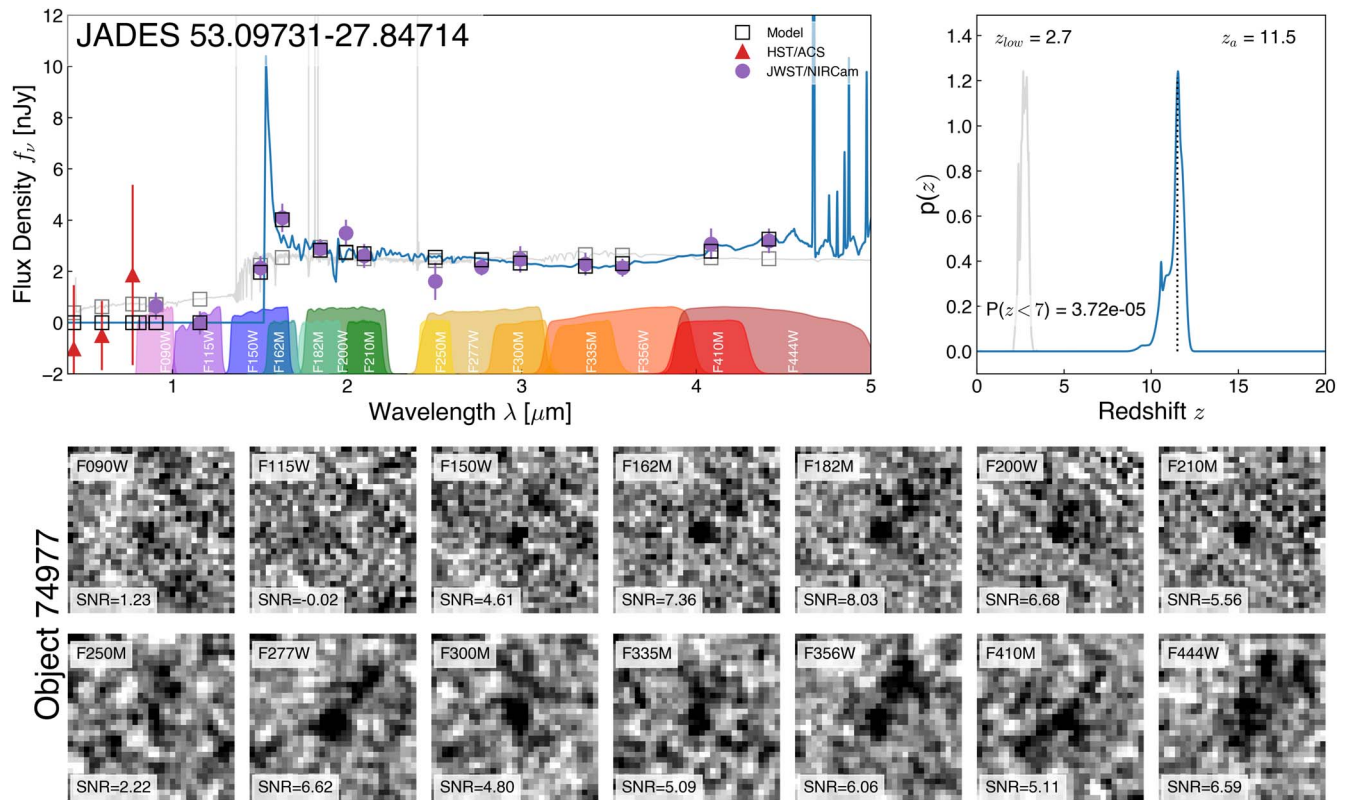


Figure 2. SED model, photometric redshift posterior distributions, and JWST/NIRCam image thumbnails for galaxy candidate JADES+53.09731-27.84714 (NIRCam ID 74977). The upper left panel shows the aperture-corrected $r = 0''1$ flux density f_ν in units of nJy of the NIRCam (purple points with 1σ uncertainties) and HST/ACS (red points with 1σ uncertainties) photometry for the object, with median photometric offset corrections applied. The best-fit SED is shown in blue, while the best-fit low-redshift solution is shown in gray. The synthetic model photometry for both models is shown as open squares, and the JWST/NIRCam filter transmission curves are shown as colored regions. The upper right panel shows the posterior distribution of photometric redshifts for the object (blue), the best-fit redshift (vertical dashed line), the photo- z posterior if only redshifts $z < 7$ are considered (light gray), and the best-fit redshifts provided as an annotation, as is the posterior probability density at redshifts below $z \sim 7$. The bottom panel shows inverted grayscale thumbnails of the 14 NIRCam filters in a 0.93×0.93 arcsec² region around each object, the stretch applied to each filter scaled with the mean value in the thumbnail. The SNR of the aperture-corrected $r = 0''1$ circular aperture photometry for each band is noted in the corresponding thumbnail. The JADES NIRCam ID is also provided on the left side of the image.

$z_{\text{phot}} = 14.51$. Owing to the observed brightness of the source and its close proximity to another lower-redshift source, NIRCam ID 183348 was rejected from their main sample. Subsequently, Williams et al. (2024) determined a lower photometric redshift $z_{\text{phot}} = 3.38$, and found the source was detected by JWST/MIRI at $7 \mu\text{m}$ in the SMILES program (PID 1207; PI: Rieke). Given the addition of our ultradeep JOF JWST/NIRCam medium-band data, we find the photometric redshift posterior distribution of NIRCam ID 183348 is sharply peaked at $z \sim 14.4$. This high-redshift peak is now much more strongly favored than low-redshift solutions as the new JOF medium-band measurements better constrain the shape and depth of the break at $\sim 1.8 \mu\text{m}$ while placing limits on strong emission lines redward of the break. While low-redshift solutions have low probability, the low-redshift photometric redshift posterior distribution is very sharply peaked near $z_{\text{low}} = 3.4$ and requires a very red object with strong emission lines in F200W and F277W. A principal concern regarding NIRCam ID 183348 is the close proximity of a neighboring galaxy (NIRCam ID 183349) that has a best-fit photometric redshift of $z_a \approx 3.4$. This alignment obviously supported the previous suspicion that NIRCam ID 183348 was also at the lower redshift. However, our analysis of the initial JOF NIRCam medium-band photometry as well as JWST/MIRI photometry (J. M. Helton et al. 2024, in preparation) further supported the higher redshift, and on that basis, the galaxy was

selected for spectroscopic follow-up. S. Carniani et al. (2024, in preparation) present a spectroscopic redshift confirmation of $z = 14.32$, and we refer the reader to that work for a detailed analysis of the properties of this intriguing galaxy. Here, we do compare the properties inferred for this galaxy along with other objects in the Main Sample measured in the same manner. We note that the photometric and spectroscopic redshift distributions are very similar, and our choice to adopt its photometric redshift distribution during the luminosity function inference has little impact on our results. We also note that gravitational lensing by the neighbor is considered by S. Carniani et al. (2024, in preparation), but they find the magnification to be small.

3.3.9. JADES+53.10762-27.86013; NIRCam ID 55733

Figure 10 shows the best-fit SED for object JADES +53.10762-27.86013 (NIRCam ID 55733; Hainline et al. 2024b). The galaxy candidate has NIRCam LW fluxes of $m_{\text{AB}} \approx 29.9$ and a best-fit redshift of $z_a \approx 14.6$. The best low-redshift solution has $z_{\text{low}} = 3.9$ with 2% of the EAZY probability, although the corresponding SED model would substantially exceed the observed F150W. We note that this object shows F162M flux at 1.1σ significance, and confirmation of this hint of a signal would negate a possible high-redshift solution.

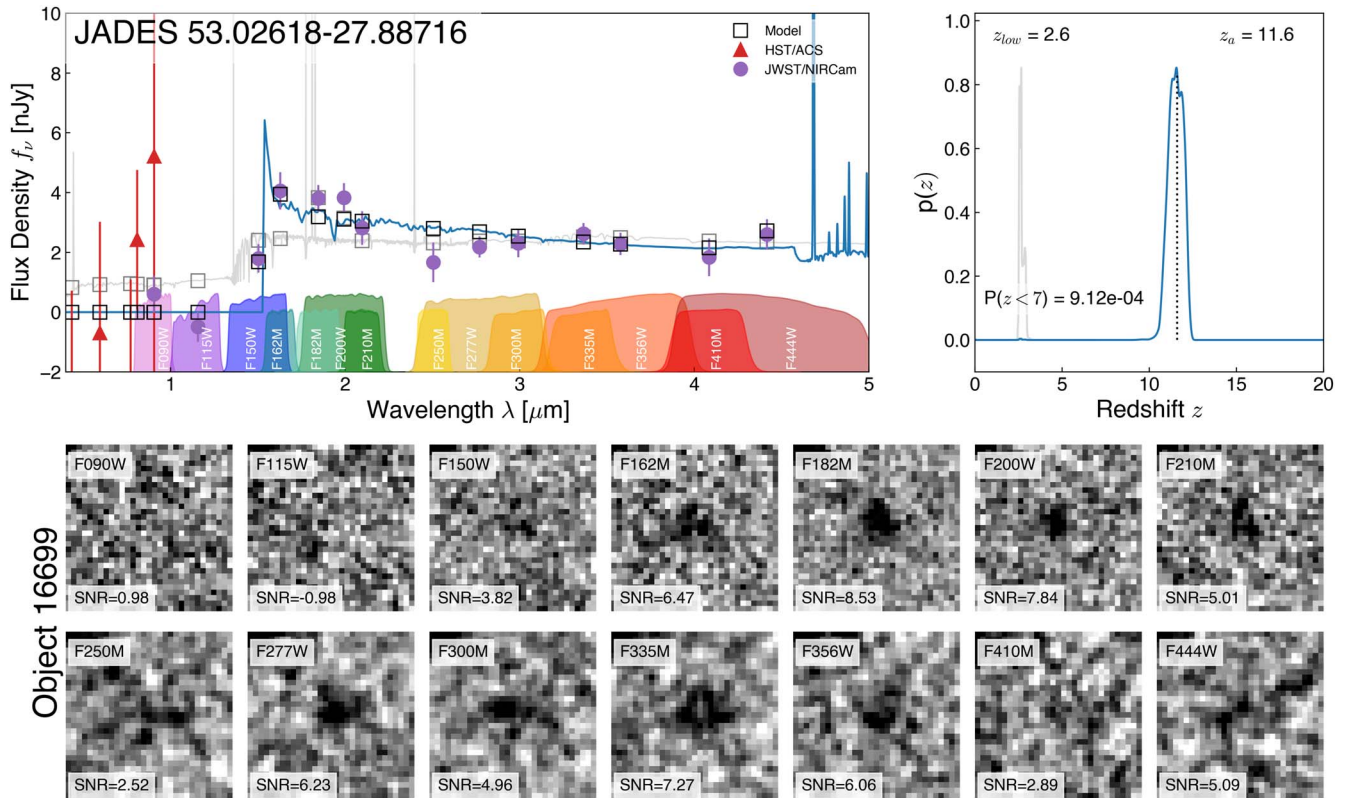


Figure 3. Same as Figure 2, but for galaxy candidate JADES+53.02618-27.88716 (NIRCam ID 16699).

3.3.10. Auxiliary Objects

We also provide SED fits for the Auxiliary candidates JADES +53.07385-27.86072 (Figure 11) and JADES+53.08468-27.86666. (Figure 12).

JADES+53.07385-27.86072 (NIRcam ID 54586) is exceedingly faint and is relegated to our Auxiliary sample by failing the minimum SNR criteria, with some LW NIRCam filters showing $m_{\text{AB}} > 30.5$ flux levels. The high-redshift posterior distribution for this object is correspondingly broader, with a peak at $z_a = 13.1$. The best low-redshift solution has $z_{\text{low}} = 3.6$.

Finally, JADES+53.08468-27.86666 (NIRCam ID 44962; Hainline et al. 2024b) is in our Auxiliary sample owing to its red SED that increases from $f_\nu \approx 3$ nJy in F182M to $f_\nu \approx 6$ nJy in F444W. The redshift posterior distribution is double-valued, with a peak at $z_a = 12.9$. The best low-redshift solution has $z_{\text{low}} = 3.5$.

4. Completeness Simulations

The detection and selection of high-redshift galaxy candidates impose limitations that reduce the completeness of a sample. To convert the number of observed galaxies satisfying the selection criteria into a measurement of the galaxy number density, the completeness of the detection and selection process need to be computed and incorporated. Below, in Section 4.1 we use simulations to characterize our detection completeness and in Section 4.2 we simulate our selection completeness. These calculations are used in Section 5 to include completeness corrections in the rest-frame UV luminosity function.

We note that the requirement to compute the completeness suggests that the detection and selection process should be algorithmic and automatable. We therefore do not apply any

cuts based on visual inspection or judgment beyond crafting the detection method described in Section 2.3 or the selection criteria presented in Section 3. This restriction allows us to simulate both the detection and selection completeness.

4.1. Detection Completeness

To compute the detection completeness of our photometric pipeline, we performed detailed source injection simulations using a wide range of input sources. First, we create a mock input galaxy catalog by drawing from randomized distributions of galaxy physical properties including redshift, SFR, stellar mass, size, Sérsic (1968) surface brightness profile index, position angle, and axis ratio. The objects are selected to have properties comparable to the $z > 8$ sources reported by Hainline et al. (2024b). We use the *Prospector* code (Johnson et al. 2021) to compute the object fluxes given their physical properties and redshift. With this mock catalog, we use the *GalSim* (Rowe et al. 2015) image simulation software to create simulated Sérsic (1968) profile objects distributed across a grid on the sky. We compute the overlap of the JOF mosaics in each filter with this grid of objects, and then add the randomized objects as injected sources in the JOF images. The result is a large set of synthetic JOF mosaics with injected sources. We can then process the images identically to the real data and attempt to discover sources.

With the injected images, we combine the LW NIRCam images as for the real data, creating an ultradeep stack. Our pipeline detection algorithm is applied to the injected mosaic stack to create a new detection catalog with simulated sources. We can then characterize the completeness of our detection method as a function of the source properties. We repeat the simulations with 10 separate realizations, such that a total of

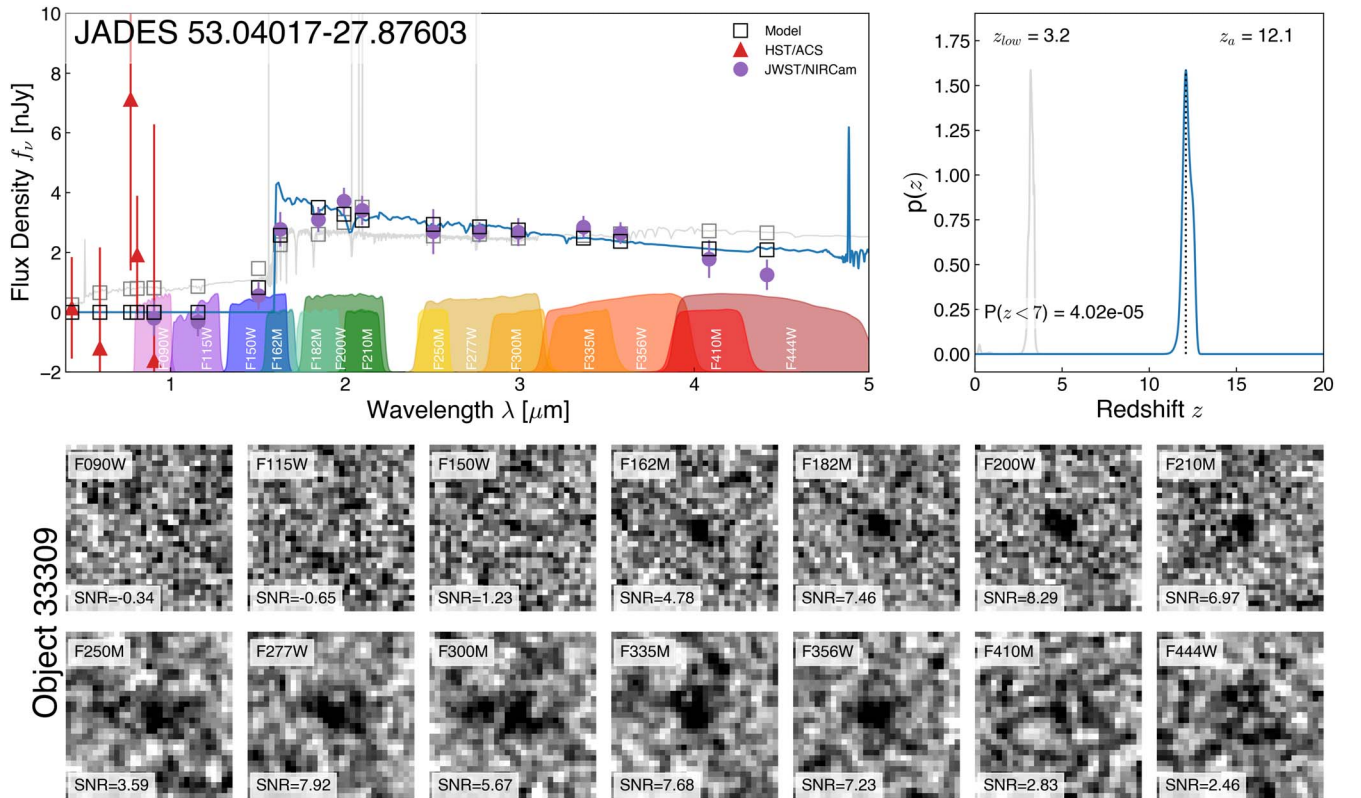


Figure 4. Same as Figure 2, but for galaxy candidate JADES+53.04017-27.87603 (NIRCam ID 33309).

115,000 injected sources with widely ranging intrinsic properties are used.

Figure 13 shows the detection completeness as a function of the two main factors affecting this completeness. The apparent brightness of the objects influence their SNR in the stacked detection image. The size of the object affects the surface brightness, which in turn determines the per pixel SNR that governs the contrast of an object of a given luminosity relative to the sky background. The detection algorithm reaches 90% completeness at around $m_{AB} \sim 30.2$ for small objects ($R_{1/2} \lesssim 0''.1$). This completeness function can be integrated into an interpolator to allow for the object completeness as a function of apparent magnitude and size to be utilized in inferring the UV luminosity function. We note that through this simulation for the JOF we find that only about 78% of the pixels are not impacted by foreground objects, which we account for in computing our effective survey volume. Given that the objects of interest are small, only several pixels across, and our detection method reaches fairly low significance ($\text{SNR} \sim 1.5$) per pixel such that the segmentations reach low surface brightnesses, we find this number to be representative of the impact of foreground sources on our detection completeness.

4.2. Selection Completeness

To simulate the selection completeness, we can use the SEDs in our mock galaxy catalog and the photometric uncertainties measured for our galaxy sample to simulate the effects of photometric noise on our selection and consequently the inferred UV luminosity function. We create a sample of two million mock galaxies with model SEDs, and induce

photometric noise with a normal scatter in each HST and JWST filter of the magnitude of our measured sky background. Our measurement uncertainties are sky dominated, so only include sky noise in our simulated fluxes. These two million noisy simulated SEDs are then provided to EAZY exactly in the same manner as our real catalog, and SED fitting is performed for each object. This enables us to estimate how the photometric noise can disrupt the mapping between true redshift and photometric redshift, and identify which redshift windows could provide nonnegligible contamination for our selection criteria. For reference, we note that in our simulations, the fraction of objects with an F200W SNR > 5 that are photometric redshift outliers with $(|z_\alpha - z_{\text{true}}| / (1 + z_{\text{true}})) > 0.1$ is 3.8%.

Figure 14 shows the completeness of selection criteria as applied to our mock galaxy catalog, as a function of the true object redshift and absolute UV magnitude. The selection proves highly complete at $M_{UV} < -18$ for redshifts $z \gtrsim 12$. At magnitudes fainter than $M_{UV} = -17.5$, the photometric noise prevents the strict elimination of low-redshift solutions such that the objects fail the $\Delta\chi^2$ selection described in 3. At the high-redshift end, the selection declines at $z \approx 20$ when the Ly α break affects F250M and our SNR requirement in that filter becomes limiting. As with the detection completeness, an interpolator can be constructed from the selection completeness and then used to correct the galaxy number counts for the lossy selection process. We note here that we define M_{UV} as the rest-frame 1500 Å UV luminosity density, computed by fitting a power law to rest-frame UV photometry and marginalizing over any covariance with the spectral slope (for more details, see Section 6.1).

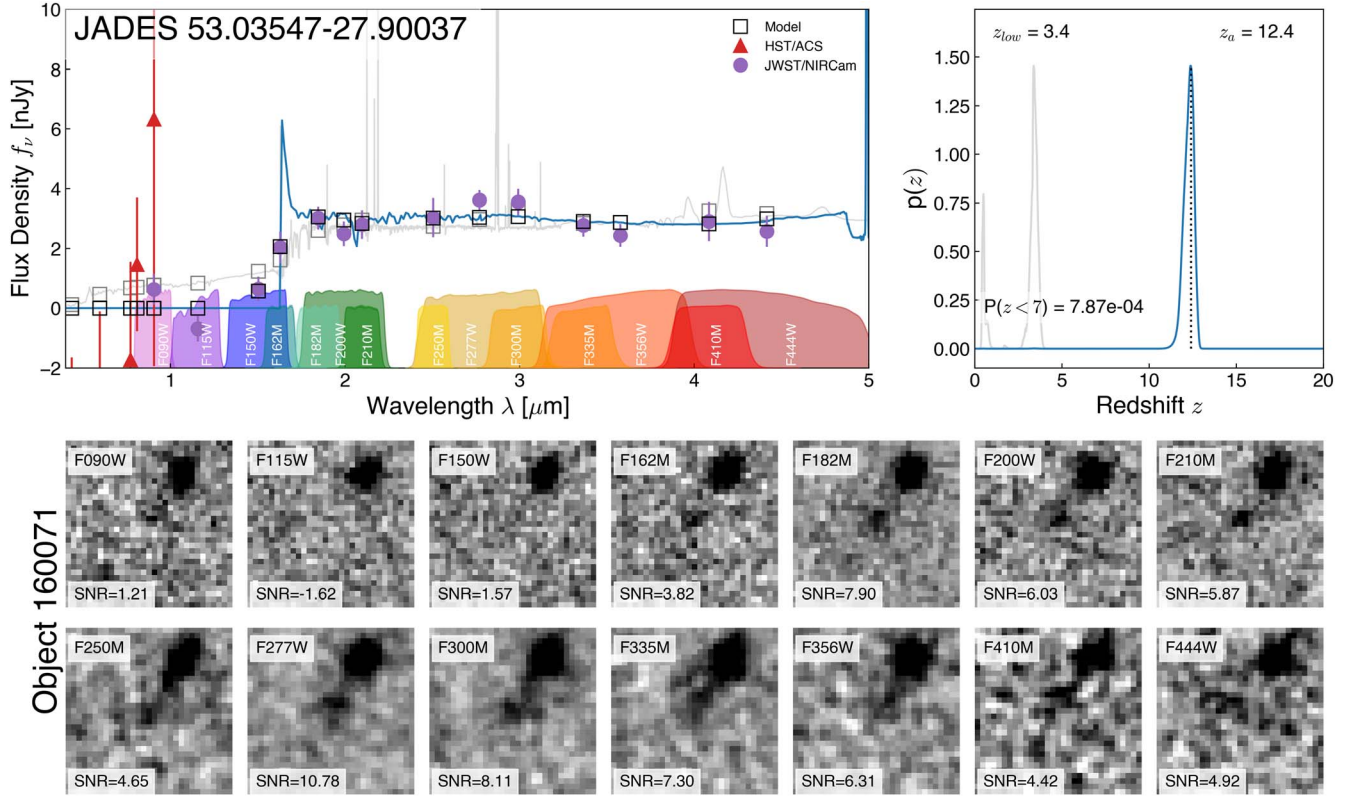


Figure 5. Same as Figure 2, but for galaxy candidate JADES+53.03547-27.90037 (NIRCam ID 160071).

5. Rest-frame Ultraviolet Luminosity Function at $z \gtrsim 12$

To compute the rest-frame UV luminosity function from our sample of galaxy candidates and our completeness calculations, we construct multiple measures of the galaxy abundance. We wish to account for several confounding effects.

First, galaxies with a range of intrinsic redshifts will contribute to the observed number counts of galaxies at a given photometric redshift. The degree of this contamination will depend on the abundance of galaxies at other proximate intrinsic redshifts whose photometric redshifts overlap with the epoch of our measurement. We must therefore account for the evolving luminosity function and mixing between populations at different redshifts.

Second, each individual galaxy has a posterior distribution for its photometric redshift. Rather than assign each galaxy to a specific redshift bin and absolute magnitude, we can allow for a posterior distribution on the photometric redshift to represent a track of inferred absolute magnitude and redshift. Each galaxy can make a fractional contribution to the UV luminosity function at redshifts where its posterior has support.

Given these considerations, we want to allow for flexibility in our representation of the UV luminosity function. We can either infer a parameterized luminosity function by computing the likelihood of observing each galaxy, given the evolving distribution of galaxy counts with luminosity and redshift, fully without binning, or we could bin in magnitude and redshift but account for the photometric redshift posterior distribution of each object. In either case, with the known individual properties of each object, we want to treat the completeness of our detection and selection methods at the per-object level rather than through binning. Below, we present both methods, where we expand on the methods used by Leja et al. (2020) to

infer the evolving stellar mass function at low redshift but now applied to the UV luminosity function evolution at high redshifts. We have tested both methods using mock galaxy samples constructed from specified luminosity functions and posterior photometric redshift distributions.

5.1. Inferring Evolving Luminosity Function Parameters

The probability of observing an object with a given true luminosity and redshift is given by the product of the redshift-dependent luminosity function $\Phi(L, z|\theta)$, the selection function $S(L, z)$, and the differential comoving volume element probed $V(z)$. We can assume the luminosity function depends on some parameters θ . Unfortunately, we do not know the true luminosity and redshift of each galaxy i , but instead estimate it from photometric data D_i , by using SED models to construct the likelihood function $\mathcal{L}(D_i | L, z)$. The likelihood of observing a galaxy with D_i must then be marginalized over the unknown true parameters

$$\mathcal{L}(D_i | \theta) \propto \int dL \int dz \mathcal{L}(D_i | L, z) \lambda(L, z | \theta), \quad (1)$$

$$\lambda(L, z|\theta) = \Phi(L, z|\theta) S(L, z) V(z), \quad (2)$$

$$\Phi(L, z|\theta) = \phi(z) (L/L_*(z))^{\alpha(z)} e^{-L/L_*(z)}. \quad (3)$$

Here $\lambda(L, z)$ is the differential number of objects expected to be selected from the survey, as a function of the true L and z . We have parameterized the luminosity function as a single Schechter function. The redshift evolution of the luminosity function can be treated with a dependence of the parameters on $(z - z_{\text{ref}})$ where z_{ref} is some reference redshift, e.g., the midpoint of the redshift range of interest. For our purposes, we adopt either simple log-linear or log-exponential evolution

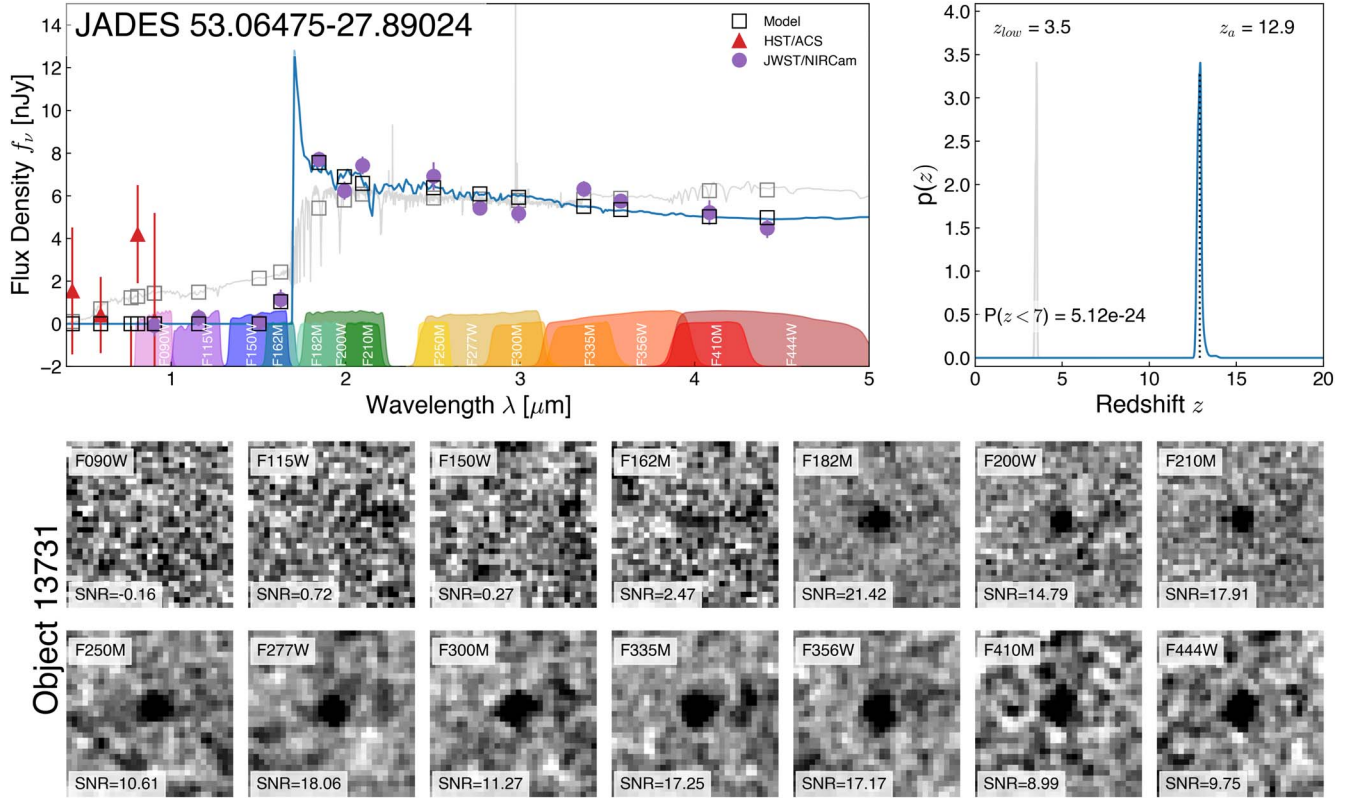


Figure 6. Same as Figure 2, but for galaxy candidate JADES+53.06475-27.89024 (NIRCam ID 13731).

with redshift. To compute the likelihood of each object marginalized over the true object redshift and luminosity we numerically integrate the marginalization integrals using samples from the probability distribution provided by EAZY

$$\mathcal{L}(D_i | \theta) \sim \sum_j w_{i,j} \lambda(L_{i,j}, z_{i,j} | \theta) / \sum_j w_{i,j}. \quad (4)$$

By drawing fair samples from the probability distributions provided by EAZY, and noting that the effective priors on z and L were uniform, each sample has equal weight $w_{i,j}$. With the ability to compute the likelihood of each object given the model, the likelihood for an ensemble of objects is then the product of the individual likelihoods. However, we must include the overall constraint given by the number of observed objects. The total expected number of selected objects is given by the integral of the product of the luminosity function and the effective volume, and the observational constraint is given by the Poisson likelihood of the actual number of observed objects²¹

$$\mathcal{L}(D | \theta) = e^{-N_\theta} \prod_i \mathcal{L}(D_i | \theta), \quad (5)$$

$$N_\theta = \int dL \int dz \lambda(L, z). \quad (6)$$

Here N_θ is the total number of observed objects. Note that for redshifts and luminosities for which our observations are

²¹ This can be derived from the treatment of the luminosity function as an inhomogeneous Poisson process; in the case that the effective rate λ is constant this reduces to the typical Poisson likelihood.

complete, the method accounts for the likelihood of nondetections given the chosen luminosity function parameter values.

5.2. Estimating a Stepwise Luminosity Function

While the method in Section 5.1 does not bin in redshift or luminosity, the observed candidate galaxies could be assigned to specific redshift and luminosity bins. If nothing else, binning allows for the measured galaxy abundance to be usefully plotted and compared with other measurements. The binned luminosity function summarizes the information retained by the unbinned parameterized luminosity function for which representing constraints on the galaxy abundance requires access to samples of the posterior distribution of luminosity function parameters.

Consider the photometric redshift posterior distribution $p_i(z)$ of a candidate galaxy i with observed apparent magnitude m_i . In the absence of photometric noise, the absolute magnitude of the object is $M_i = m_i - DM(z)$, where $DM(z)$ is the cosmological distance modulus including a K-correction. Accounting for photometric noise, we will instead have some distribution of absolute magnitudes $p(M_i | m_i, z)$ for each object at a given photometric redshift. The distribution of inferred absolute magnitudes in some redshift bin z_1 to z_2 is

$$p(M_i | z_1, z_2) = \int_{z_1}^{z_2} dz \int dm_i p(M_i | m_i, z) p(z). \quad (7)$$

The contribution of a galaxy to an absolute magnitude bin would then be

$$N_i(M_1, M_2, z_1, z_2) = \int_{M_1}^{M_2} p(M_i | z_1, z_2) dM_i. \quad (8)$$

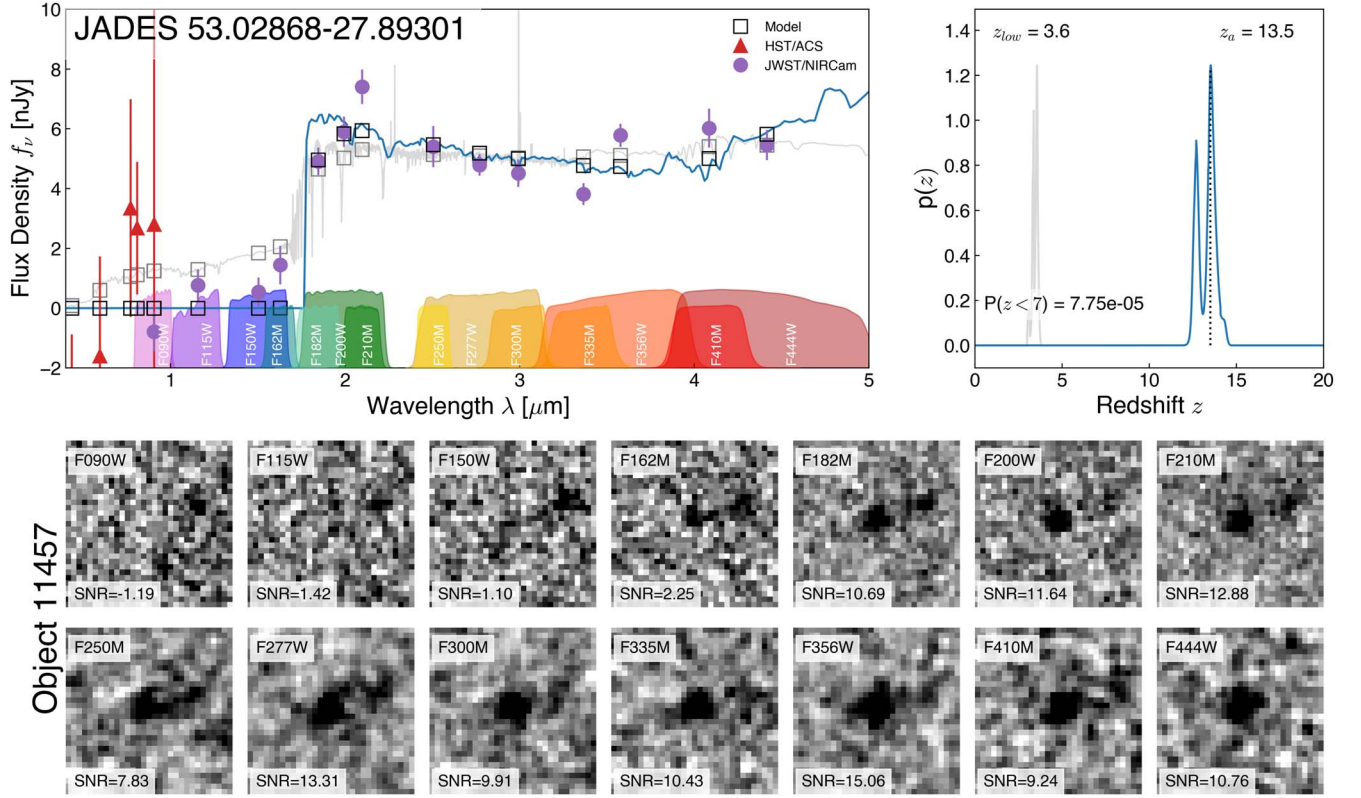


Figure 7. Same as Figure 2, but for galaxy candidate JADES+53.02868-27.89301 (NIRCam ID 11457).

The total number density per magnitude n_j in a magnitude bin $M_1 < M_j < M_2$ would then be

$$n_j(M_1, M_2, z_1, z_2) = \frac{\sum_i N_i(M_1, M_2, z_1, z_2)}{(M_2 - M_1) V_j}, \quad (9)$$

where V_j is the average effective volume in the bin, allowing for the completeness to vary for each object i . In practice, evaluating these equations involves summing over samples from the photometric posterior distributions of the galaxies while accounting for samples that lie outside the redshift bin to enforce the posterior normalization constraint $\int p(z) dz = 1$. We note that when computing the samples in M_{UV} and z , to compute M_{UV} we use the 1500 Å rest-frame flux computed in the appropriate JWST filter given a putative redshift z . When computing M_{UV} , we use the total fluxes computed from the `Forcepho` morphological decompositions.

Procedurally, for each redshift bin we take all ordered M_{UV} samples and separate them into bins whose edges are set to maintain a comparable number of samples per bin. We sum the number of samples in each bin and divide by the total number of samples across all galaxies, which provides the (noninteger) number of galaxies per bin. The average completeness in the bin is computed from the per-object selection and detection completeness based on the object properties and the fraction of pixels in the image not covered by foreground sources. We then divide the number of galaxies in each bin by the bin width, the completeness, and the volume to get the number density. The uncertainties for each bin are estimated from number count statistics.

While we report our stepwise estimate, which accounts for photometric scatter between magnitude bins and variable completeness, we consider these measurements estimated

checks on the inferred luminosity function constraints described in Section 5.1 that do not bin in either redshift or magnitude and additionally account for potential contamination from proximate redshifts and the evolving shape of the luminosity function with redshift. We emphasize here that our formal derived constraints on the luminosity function are provided through our inference procedure in the form of the computed posterior distributions of the parameters of our model evolving luminosity functions.

5.3. Luminosity Function Constraints

Given the measured properties of our sample galaxies, their photometric redshift distributions $p(z)$, and the method described in Section 5.1, we can compute marginalized constraints of an evolving UV luminosity function once we adopt a parameterized form.

For the luminosity function, we adopt a redshift-dependent Schechter (1976) function

$$\phi_{UV}(M_{UV}, z) = 0.4 \log_{10} \phi_{*}(z) [10^{0.4(M^{*} - M_{UV})}]^{\alpha+1} \times \exp[-10^{0.4(M^{*} - M_{UV})}], \quad (10)$$

where the redshift-dependent normalization $\phi_{*}(z)$ can be further parameterized. Our fiducial choice for the normalization evolution is

$$\log_{10} \phi_{*}^l(z) = \log_{10} \phi_{*,0} + \eta(z - z_0). \quad (11)$$

We will refer to z_0 as the reference redshift, which we will take fixed at $z_0 = 12$ unless otherwise noted. The default parameters of the model then include $\vec{\theta} = [M^{*}, \alpha, \phi_{*,0}, \eta]$, with the characteristic magnitude M^{*} , the faint-end slope α , the normalization at the reference redshift $\phi_{*,0}$, and the log-linear

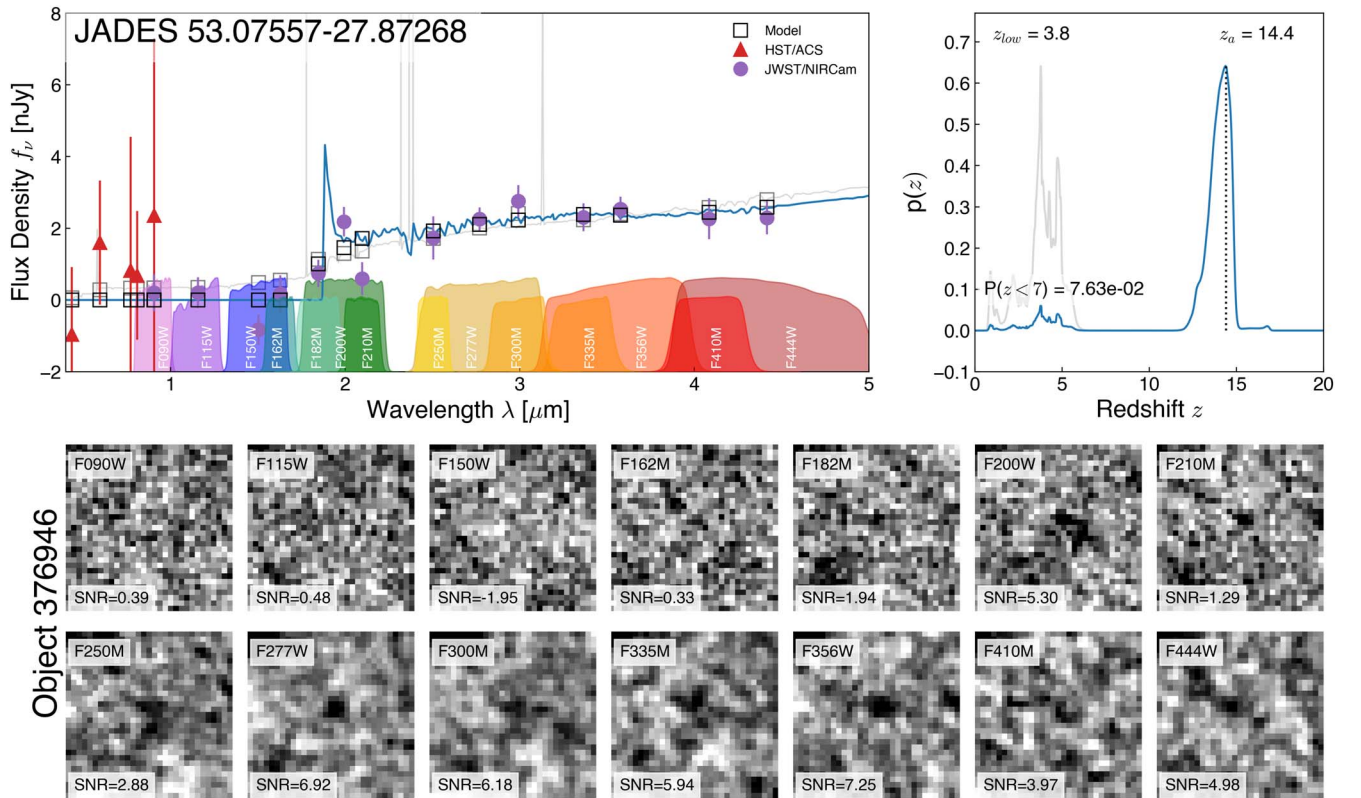


Figure 8. Same as Figure 2, but for galaxy candidate JADES+53.07557-27.87268 (NIRCam ID 376946).

rate of change with redshift η . In practice, we fit in maggies $l = -0.4M_{UV}$ and then convert to absolute magnitudes after inference. We adopt log-uniform priors for $\phi_{*,0}$ and η , a uniform prior in magnitude, and a uniform prior in α . The priors are reported in Table 6, along with our inferred constraints on the parameters. We emphasize again that information from all redshifts where the selection function has nonnegligible support is included by our inference procedure, which accounts both for regions of redshift and magnitude space with detections and those absent samples that could have been detected if present. The effective redshift range where our model is informative for the luminosity function is mostly set by the selection completeness (Figure 14), or roughly $z \sim 11$ – 20 . We present the full posterior distributions on the parameters in Figure 15. We here emphasize that the clear covariance between ϕ_* and M^* mostly acts to keep the luminosity density $\rho_{UV} \propto L^* \phi_*$ roughly constant at a given redshift. This feature is reflected in our constraints on ρ_{UV} shown in Figure 17.

Since we constrain the abundance of galaxies at all selected and detectable redshifts and magnitudes simultaneously, evaluating the luminosity function at any one redshift requires computing the marginal distribution of the luminosity function (Equation (10)) over the posterior distribution of parameters for a given redshift and range of absolute magnitudes. At each z and M_{UV} , Equation (10) is evaluated for all posterior samples, and the cumulative distribution of ρ_{UV} weighted by the sample weights w_k constructed. Figure 16 shows the marginal constraint on the UV luminosity function at redshift $z = 12$, with the 16%–84% of ϕ_{UV} shown as a shaded region and the median ϕ_{UV} shown as a white line. We also show the median

inferred ϕ_{UV} at $z = 14$ as a light gray line. Note that none of these ϕ_{UV} percentiles are guaranteed to follow Equation (10) individually, but we do report the marginalized constraints on the luminosity function parameters in Table 6. We also show our stepwise luminosity function estimates computed in redshift bins of $11.5 < z < 13.5$ and $13.5 < z < 15$. These stepwise luminosity function measures are reported in Table 7.

In Figure 16, we also show $z \sim 12$ – 14 luminosity function determinations reported in the literature. These measurements include the $z \sim 12$ data from Harikane et al. (2024), Pérez-González et al. (2023a), Harikane et al. (2023), and Willott et al. (2024); the Adams et al. (2024) constraints at $z \sim 12.5$; $z \sim 13$ measurements from Donnan et al. (2023a) and McLeod et al. (2024); and the $z \sim 14$ determinations from Finkelstein et al. (2024). The median luminosity function constraints inferred from our sample and our forward-modeling approach agree with the available observations to within about 1σ , except for the $z \sim 14$ constraints from Finkelstein et al. (2024), which lie above our inference. We note here that the $z \sim 11$ luminosity function constraints from Donnan et al. (2023a), McLeod et al. (2024), and Finkelstein et al. (2024) lie above our 84% inference of the $z = 12$ luminosity function, and that our selection function (Figure 14) by design removes $z \sim 11$ galaxies from our sample. We also emphasize that our results are completely independent of the other data shown in Figure 16.

5.3.1. Luminosity Density Evolution

Given the evolving luminosity function parameters inferred given the sample properties, the UV luminosity density evolution $\rho_{UV}(z)$ can be computed. Figure 17 presents the marginalized constraints on the UV luminosity density evolution. Shown are 16%–84% (jade-shaded region) and

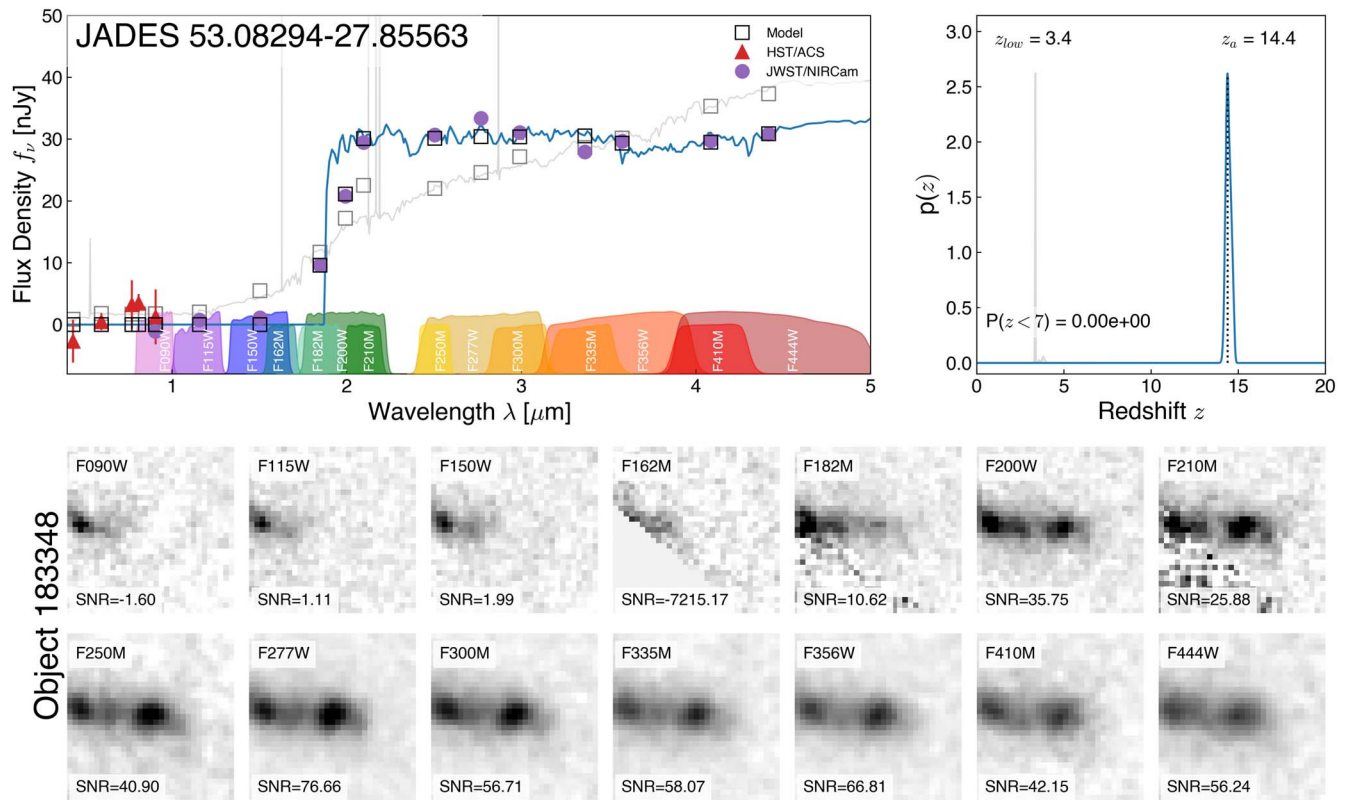


Figure 9. Same as Figure 2, but for galaxy JADES+53.08294-27.85563 (NIRCam ID 183348). We note this object has been discussed previously in Hainline et al. (2024b) and Williams et al. (2024), and spectroscopically confirmed by S. Carniani et al. (2024, in preparation). The F162M data for this object have been omitted because of data quality issues.

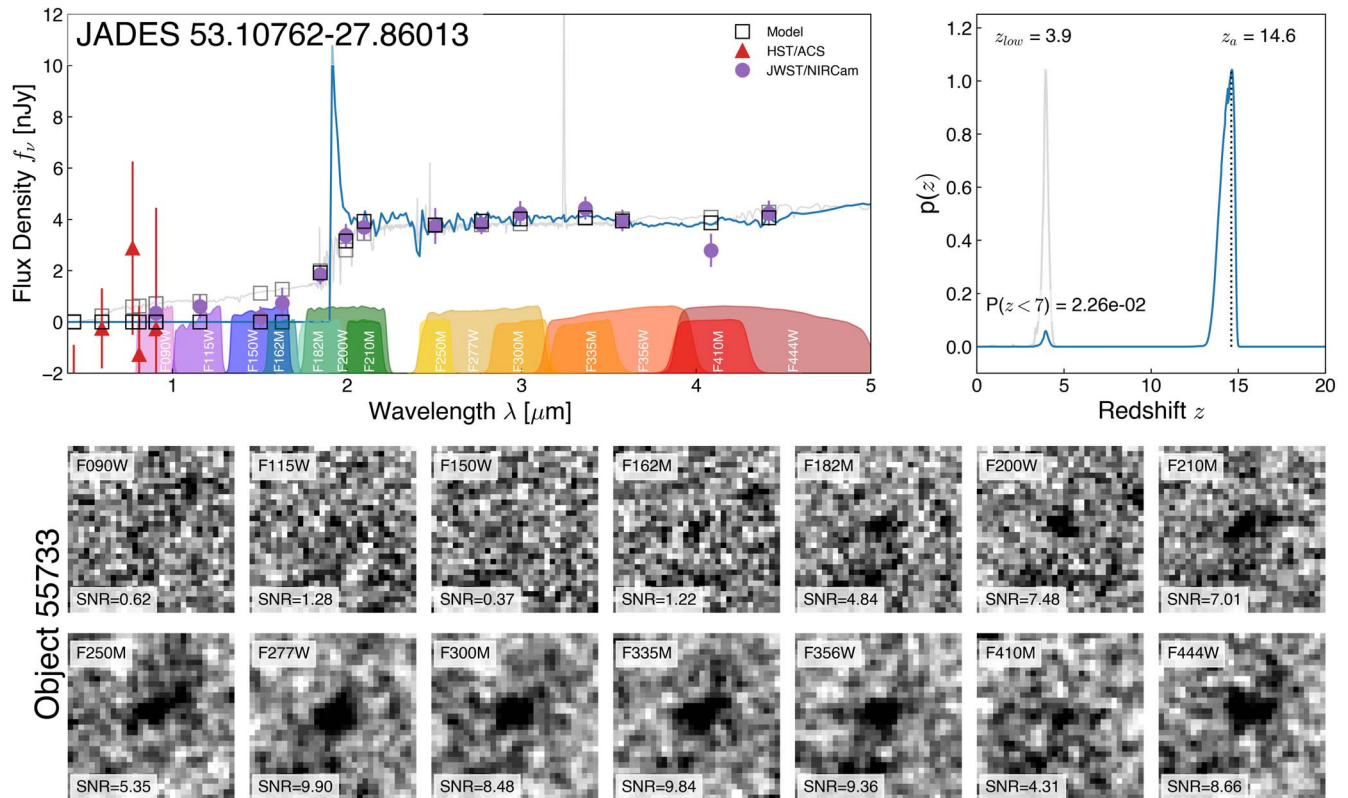


Figure 10. Same as Figure 2, but for galaxy candidate JADES+53.10762-27.86013 (NIRCam ID 55733).

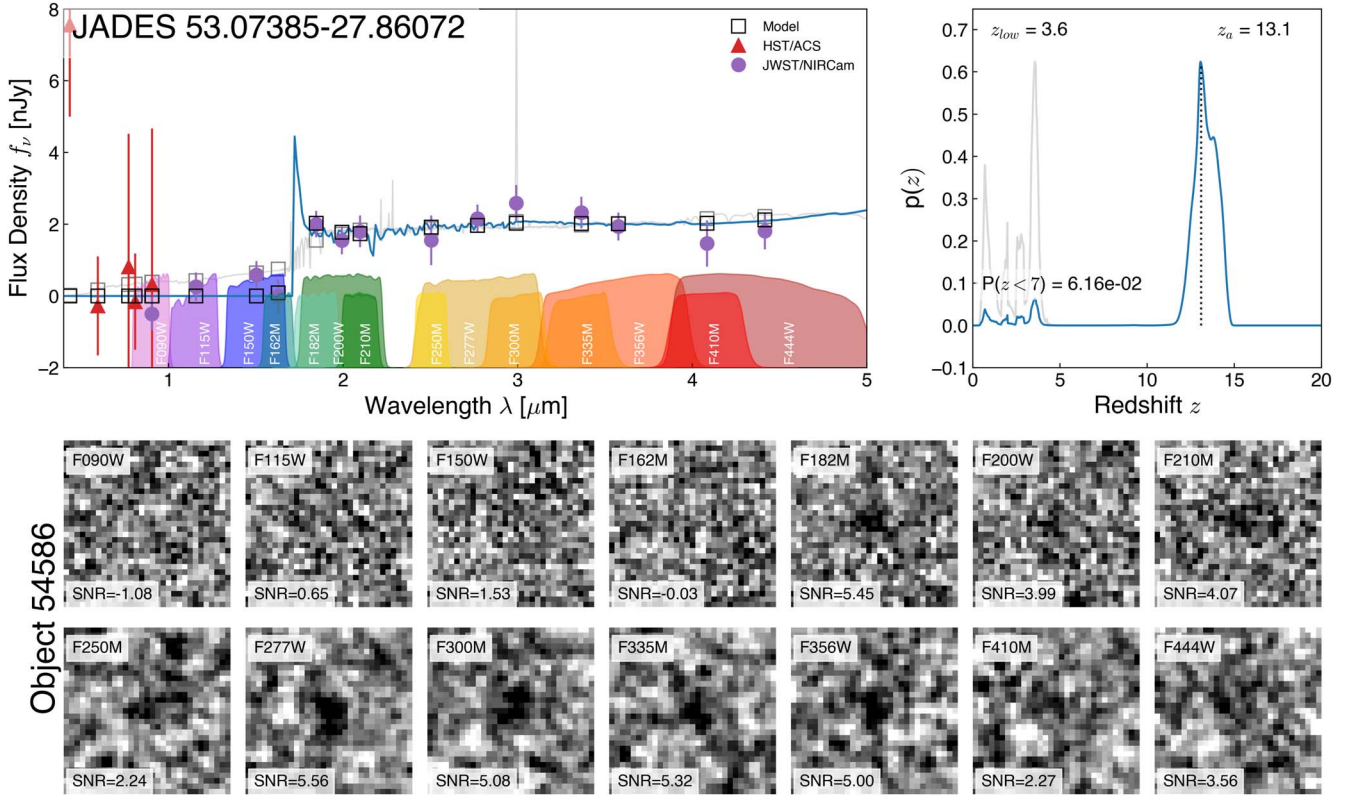


Figure 11. Same as Figure 2, but for Auxiliary galaxy candidate JADES+53.07385-27.86072 (NIRCam ID 54586).

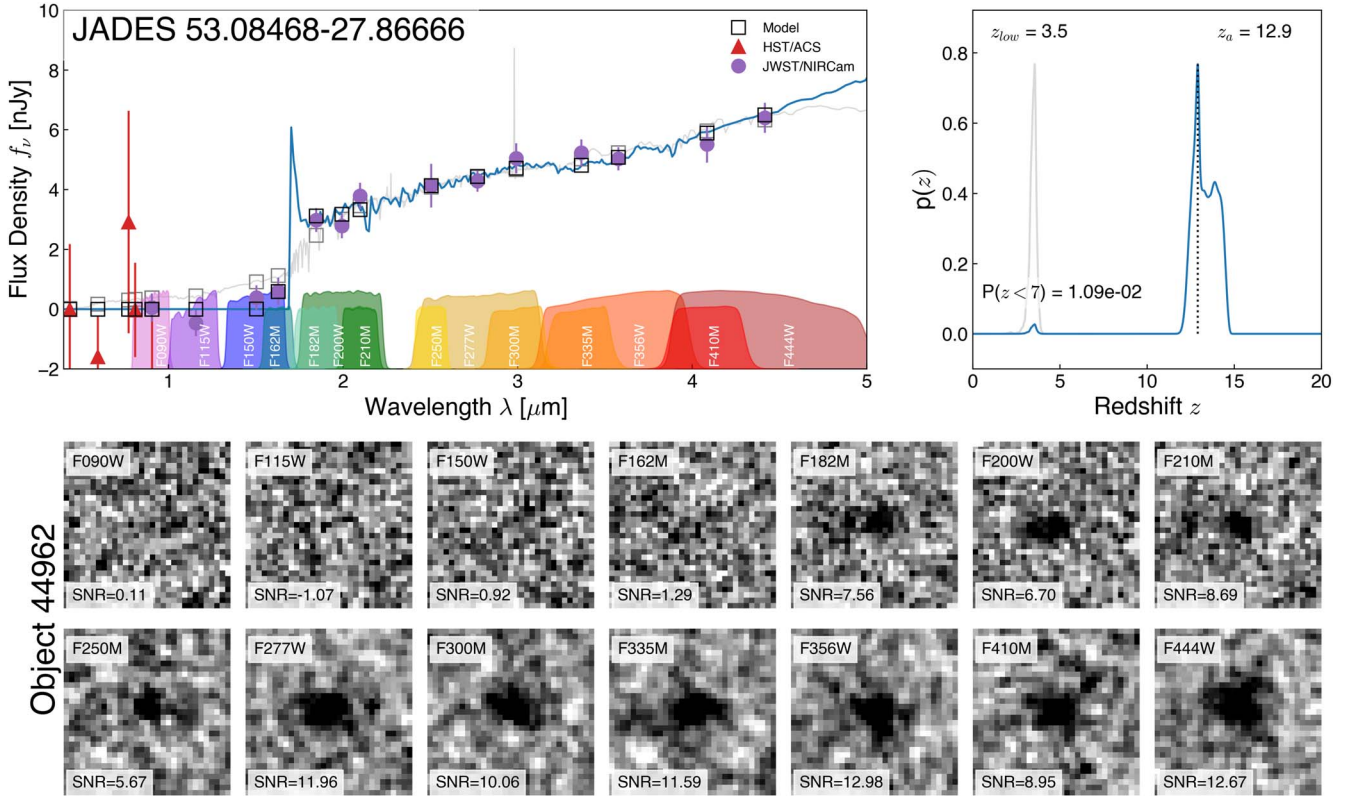


Figure 12. Same as Figure 2, but for Auxiliary galaxy candidate JADES+53.08468-27.86666 (NIRCam ID 44962).

median ρ_{UV} (white line) integrated to $M_{UV} < -17$, along with measured (left panel) or extrapolated (right panel) constraints on $M_{UV} < -17$ from the literature. Our measurements have

sensitivity to objects at redshifts $11 \lesssim z \lesssim 20$, and we indicate the luminosity density evolution inferred for the model represented by Equations (10) and (11). As the figure shows,

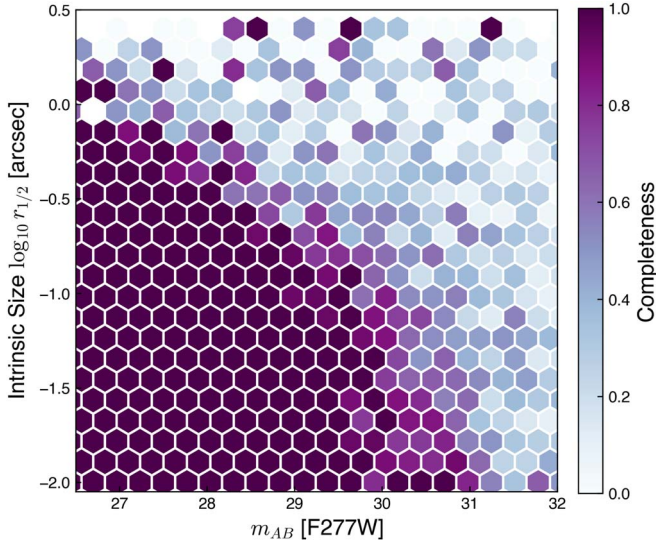


Figure 13. Detection completeness in our JOF analysis as a function of intrinsic half-light radius and F277W apparent magnitude. The detection method is complete for small objects and bright magnitudes, and the differential completeness reaches about 90% at F277W \approx 30.2 AB for small objects. Shown is a 2D normalized histogram of object size and flux indicating the fraction of sources with such properties detected by the pipeline. The method becomes highly incomplete fainter than $m_{AB} \sim 31$ or for half-light radii above about half an arcsecond. Owing to pixels covered by foreground sources, the maximum detection completeness will be reduced to $\sim 78\%$ of that shown here.

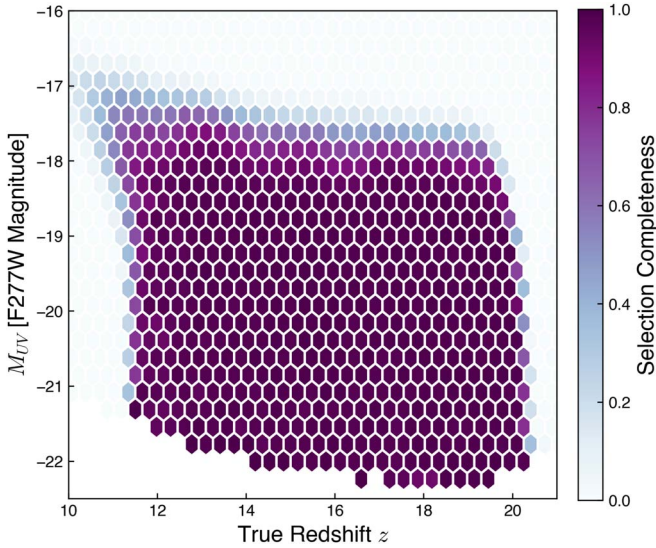


Figure 14. Completeness of our selection criteria as a function of galaxy redshift and absolute magnitude. For bright objects, the selection criteria described in Section 3 produce a substantially complete sample. For fainter objects, the $\Delta\chi^2$ criterion fails as the photometric noise prevents the SED-fitting procedure from distinguishing robustly between high and low photometric redshifts.

we infer that the UV luminosity density declines at high redshift at a rate of $\eta \equiv d \log \phi_*/dz \approx -0.2$ per unit redshift. Between $z=12$ and $z=14$, we therefore infer that the luminosity density declines by a factor of $10^{-0.2(14-12)} \approx 2.5$. Within our statistical uncertainties, this inference agrees with almost all the literature determinations including Ishigaki et al. (2018), Bouwens et al. (2022), Harikane et al. (2024), Pérez-González et al. (2023a), Adams et al. (2024), Donnan

Table 6
Luminosity Function Marginalized Parameter Constraints

Parameter	Prior	Constraint	Constraint	Constraint
$\log_{10} \phi_{*,0}$ ^a	$\mathcal{U}(-8, -2)$	-6.39	-5.22	-4.24
M^* ^b	$\mathcal{U}(-17, -24)$	-24.95	-22.80	-20.71
η ^c	$\mathcal{U}(-3, 3)$	-0.29	-0.20	-0.13
α	$\mathcal{U}(-3, -1)$	-2.16	-1.79	-1.43

Notes.

- ^a The lower limit on the luminosity function normalization is not well constrained, but the 95% upper limit is $\log_{10} \phi_{*,0} < -3.84$.
- ^b The 95% upper limit on the characteristic magnitude is $M^* < -19.9$.
- ^c We constrain the evolution parameter to be $\eta < -0.08$ at 95%.

et al. (2023b), Harikane et al. (2023), Leung et al. (2023), McLeod et al. (2024), and Willott et al. (2024). The constraints at $z \sim 11$ from Finkelstein et al. (2024) agree with our results, but their $z \sim 14$ point lies above our constraints albeit with large uncertainties. If we extrapolate the UV luminosity evolution inferred by our model, we find good agreement with the literature measurements back to $z \sim 8$ (e.g., Ishigaki et al. 2018; Bouwens et al. 2022; Pérez-González et al. 2023a; Adams et al. 2024; Willott et al. 2024). Also shown in Figure 17 is the corresponding evolution in the cosmic SFR density ρ_{SFR} , using the approximate conversion from ρ_{UV} of $\kappa_{UV} = 1.15 \times 10^{-28} M_{\odot} \text{ yr}^{-1} \text{ erg}^{-1} \text{ s Hz}$ from Madau & Dickinson (2014). For comparison, we also show the Madau & Dickinson (2014) model for the evolving cosmic SFR density.

5.4. Caveats

Of course, with only nine objects at these extreme distances and depths, there are important caveats to consider about the luminosity function measurement. First, most of our objects are photometric candidates, and despite the closer spacing of the medium bands and our care in selection, we consider it possible that some might be lower-redshift interlopers. A Ly α break at $z = 14$ falls at the same wavelength as a Balmer break around $z \approx 4$. We stress that false positives would likely have a redshift distribution that falls less slowly than the true Ly α break population, so a population of false positives will typically cause the luminosity function to appear to evolve more shallowly at extreme redshifts. However, the success of our selection method in providing a photometric redshift for NIRCcam ID 183348 of $z = 14.32$ that was confirmed by S. Carniani et al. (2024, in preparation) provides some evidence that our highest-redshift candidates could bear out.

Since the remaining candidates at $z > 13.5$ have some imperfections in their cases, as discussed in Section 3.3, and to illustrate the relative impact of the highest-redshift objects on our inferences, we consider the impact on the luminosity function estimate if we were to ignore the $z > 14$ objects. Removing these objects makes the inferred evolution of the luminosity function notably steeper, which we show through the UV luminosity density evolution in Figure 17 where the light jade region and gray line report the marginalized 16–84% credibility interval and median ρ_{UV} , respectively. Since the fiducial model assumes an evolution $\phi_*^l(z)$ that has a log-linear dependence on redshift, the ρ_{UV} inferred by the model beyond the redshift of our observed sample can in principle be artificially inflated by the inferred trend at $z \sim 12-14$. Instead, when removing the $z > 14$ objects, we explore a more rapid

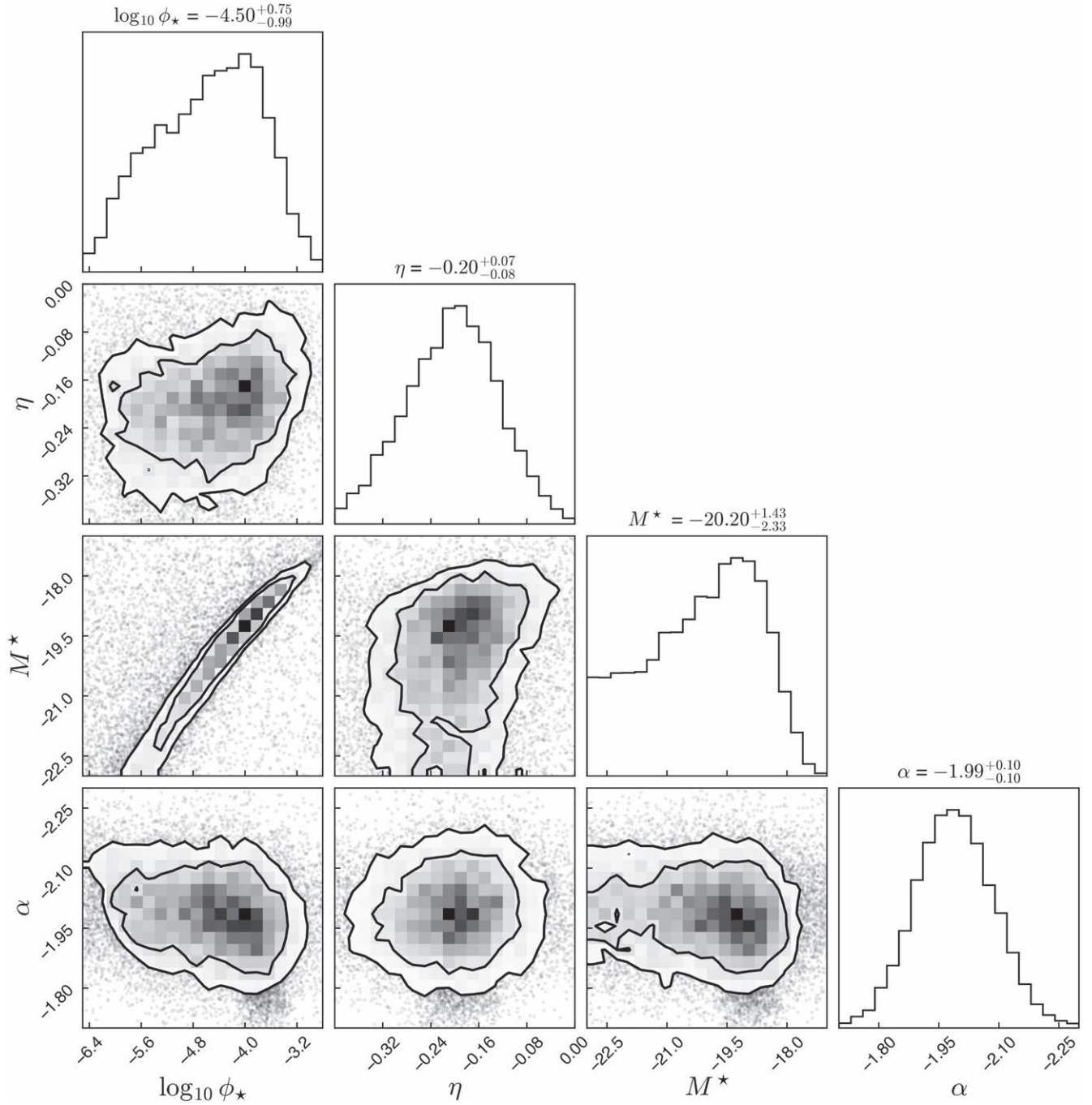


Figure 15. Posterior distributions of the evolving luminosity function parameters. Shown are the posterior distributions for the luminosity function normalization $\log_{10} \phi_*$ [units of $\text{Mpc}^{-3} \text{mag}^{-1}$], the normalization evolution parameter η , the characteristic magnitude M^* in absolute magnitude, and the faint-end slope α . Contours represent the 68% and 90% enclosed probabilities for each parameter. The marginalized posterior distributions for each parameter are shown at the top of each column, along with the 16%, 50%, and 84% marginal constraints (see also Table 6). The lower limits on ϕ_* and M^* are not well constrained, but we constrain at 95% probability that $\log_{10} \phi_* < -3.84$ and $M_* < -19.9$. We note that $\eta < 0$ with $>95\%$ probability, indicating that we infer a declining luminosity density at $z > 12$.

decline given by

$$\log \phi_*^e(z) = \log(\phi_{*,0}) \times \exp[(z - z_0)/h_\phi]. \quad (12)$$

This model enables a log-exponential drop in the galaxy abundance. Indeed, without the $z > 14$ objects the inferred ρ_{UV} would drop much more rapidly than in the fiducial model based on the Main Sample. For reference, by $z \sim 16$ the difference between the two inferences is more than an order of magnitude. Of course, given the small number statistics, we are also

sensitive to the impact of a single false negative. If any of the remaining Auxiliary Sample objects in Section 3.3 were to prove out, the luminosity function would surely rise.

5.5. Comparison with Halo Abundance and Large-scale Structure

The large-scale structure of the Universe is expected to present a substantial cosmic variance uncertainty given the small size of this field. High-redshift galaxies likely live in rare

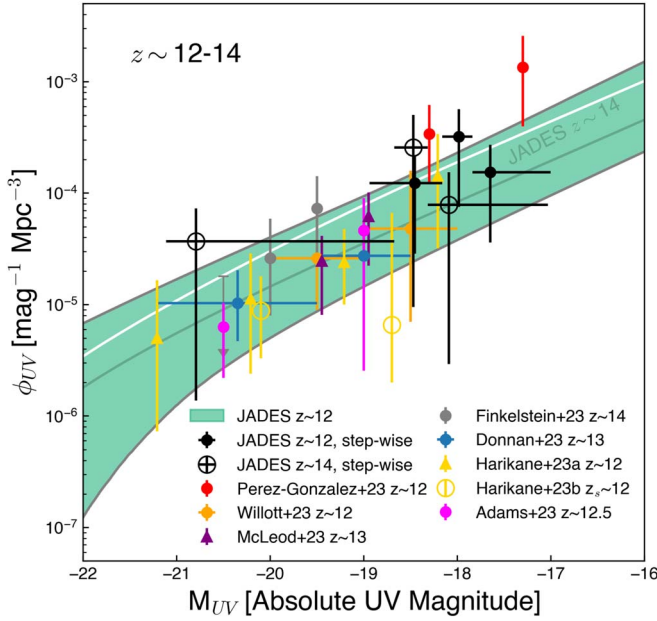


Figure 16. UV luminosity function at $z \sim 12$ inferred from the JOF. Using the method described in Section 5.1, we compute the marginalized constraints on the UV luminosity function inferred from galaxies discovered in the JOF with photometric redshift distributions that overlap the redshift range $11.5 < z < 13.5$. We account for photometric scatter, the photometric redshift distribution of each object, the selection completeness for each object, and potential contamination from proximate redshifts. The 16%–84% marginal constraints on the abundance ϕ_{UV} as a function of absolute UV magnitude M_{UV} are shown as a jade-shaded area and the median $\phi_{UV}(M_{UV})$ is shown as a white line. For comparison, we also compute stepwise luminosity function constraints as described in Section 5.2 at $z \sim 12$ (solid black points) and at $z \sim 14$ (open black circles). These stepwise estimates agree with the inferred ϕ_{UV} , but the continuous constraints represent our results for the UV luminosity function. We also show a variety of constraints from the literature at comparable redshifts (colored points), and note that none of these data were used to aid our inference of the UV luminosity function.

Table 7
Stepwise Luminosity Function

M_{UV}	$\phi_{UV} [10^{-4} \text{ mag}^{-1} \text{ Mpc}^{-3}]$
$11.5 < z < 13.5$	
$-18.5^{+0.18}_{-0.48}$	1.22 ± 0.94
$-18.0^{+0.14}_{-0.18}$	3.20 ± 2.46
$-17.6^{+0.65}_{-0.19}$	1.54 ± 1.18
$13.5 < z < 15$	
$-20.8^{+2.12}_{-0.32}$	0.371 ± 0.357
$-18.4^{+0.16}_{-0.50}$	2.56 ± 2.46
$-18.1^{+1.13}_{-0.23}$	0.783 ± 0.754

Note. The ranges listed for each M_{UV} reflect the widths of the magnitude bins, which are determined by the distribution of photometric redshift posterior samples for the objects contributing to each bin.

halos of high mass for their epoch, leading to a large clustering bias and substantial number density fluctuations. To investigate this, we utilize the halo catalog from a cold dark matter simulation performed by the Abacus N -body code as part of the AbacusSummit suite (Garrison et al. 2021; Maksimova et al. 2021). This simulation used 6144^3 particles in a $300 h^{-1} \text{ Mpc}$ box, resulting in a particle mass of $1.5 \times 10^7 M_{\odot}$, and a force softening of 21 comoving kpc. Halos were found using the

CompaSO algorithm (Hadzhiyska et al. 2021). While this simulation has high accuracy, we caution that the measurement of halo mass always depends on the halo-finding algorithm; we focus here on the relative trends across redshift and on the clustering.

In Figure 18, we compare our luminosity function measurements to the cumulative halo mass function as a function of redshift. One sees that if the shallow luminosity function is correct, then matching the abundance of these galaxies to the abundance of the most massive halos would require a strongly evolving halo mass. On the other hand, if one were to discard the objects at $z > 14$, then the result is more similar to the abundance of a constant mass, roughly of $10^{10} M_{\odot}$. Of course, the galaxies may live in less massive halos, with a scatter between luminosity and mass (e.g., Sun et al. 2023; Shen et al. 2024); indeed, some scatter is inevitable (Pan & Kravtsov 2023). In what follows, we therefore consider the properties of halos with virial masses of $10^{9.7} M_{\odot}$, about 340 particles, which has comparable abundance to our galaxy sample at $z \sim 12$ –14.

We then calculate the variation within the simulation of regions similar in size to the JOF. We use pencil-shaped regions of $6 h^{-1} \text{ Mpc}$ square, roughly $3'$ at $z \sim 12$, with a depth appropriate to $\Delta z = 1$. We find that at $z = 12$ (11.5–12.5), there is an average of 8.3 halos above our mass threshold in a region, but with a standard deviation of 5.6. At $z = 13$, this abundance drops to 2.3 ± 2.3 ; at $z = 14$, the abundance drops further to $0.7^{+1}_{-0.7}$. The distribution of halo number counts becomes noticeably skewed, and by $z = 14$ we find that 6% of regions have ≥ 3 halos. Hence, we find that unless the host halos are much less massive (and their luminosities much more variable), the large-scale structure contributes an error at least as large as the Poisson error. We caution that this uncertainty could impact the observed rate of decline of the UV luminosity density, given our area, and motivates further studies over larger fields. However, to combat other systematics such studies should also leverage the depth and filter coverage comparable to that afforded by the JOF, which is challenging given the necessary exposure time.

Finally, we note that we have neglected the effect of magnification by gravitational lensing in our inference of M_{UV} . While none of our candidates show obvious lens morphology, the high-luminosity tail of the high-redshift luminosity function will likely be enhanced by lensing (e.g., Wyithe et al. 2011; Mason et al. 2015; Ferrami & Wyithe 2023), which might affect interpretations of the luminosity function in the context of theories of galaxy formation.

6. Physical Properties of the High-redshift Population

Beyond the abundance and UV luminosities of these $z \gtrsim 12$ galaxies, the physical properties of the galaxies are of particular interest for understanding the process of galaxy formation at the earliest epochs. With the high-quality space-based optical–infrared photometry available in the JOF, physical properties of the high-redshift galaxy stellar populations can be inferred.

6.1. Rest-frame Ultraviolet Magnitude and Spectral Slope

Given the dramatic distances to these objects, the photometry obtained in the JOF primarily probes only their rest-frame UV spectra. Using common PSF images and aperture-corrected Kron photometry as a proxy for the total fluxes, we

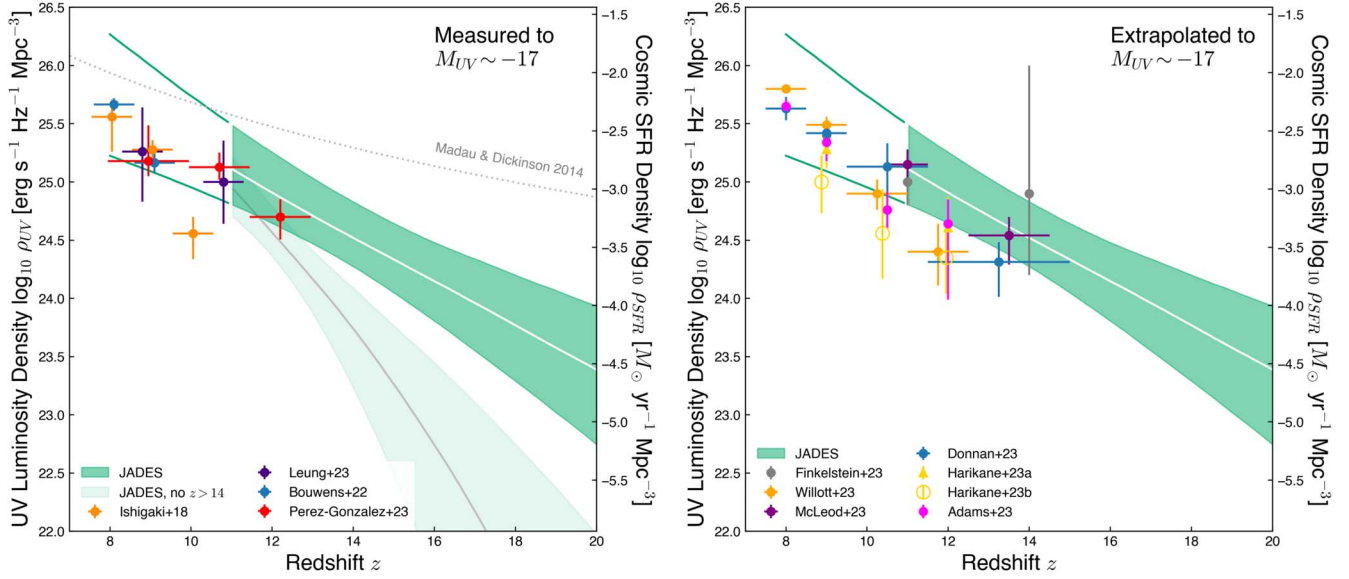


Figure 17. Evolution of the UV luminosity density $\rho_{UV}(M_{UV} < -17)$ with redshift derived from the JOF sample. Shown are literature values for $\rho_{UV}(z)$ measured (left panel) or extrapolated (right panel) to $M_{UV} < -17$. In both panels, the shaded jade region shows the 16% and 84% marginal constraints on the luminosity density computed from the posterior samples of the evolving luminosity function inference, as well as the median luminosity density with redshift (white line). These constraints model a linear evolution in $\log_{10} \phi_*$ and include a permissive prior on the faint-end slope α . Overall, our constraints agree well with the prior literature results even though our inference is completely independent. The dark green lines extending to $z \sim 8$ show the low-redshift extrapolation of the inferred $\rho_{UV}(z)$ evolution, while the shaded region indicates the redshift range where our detection and selection completeness is nonnegligible. We also indicate an approximate cosmic SFR density (right axis; units of $M_{\odot} \text{ yr}^{-1} \text{ Mpc}^{-3}$) using the conversion $\kappa_{UV} = 1.15 \times 10^{-28} M_{\odot} \text{ yr}^{-1} \text{ erg}^{-1} \text{ s Hz}$, and show the Madau & Dickinson (2014) model (left panel; dotted line). For comparison, in the left panel, we show the corresponding constraint if the JOF high-redshift galaxies and candidates at $z > 14$ are excluded and $\log_{10} \phi_*$ is fit with an exponential evolution. In this case, we would infer the light jade region (16%–84% marginal constraint), shown with the gray line (median).

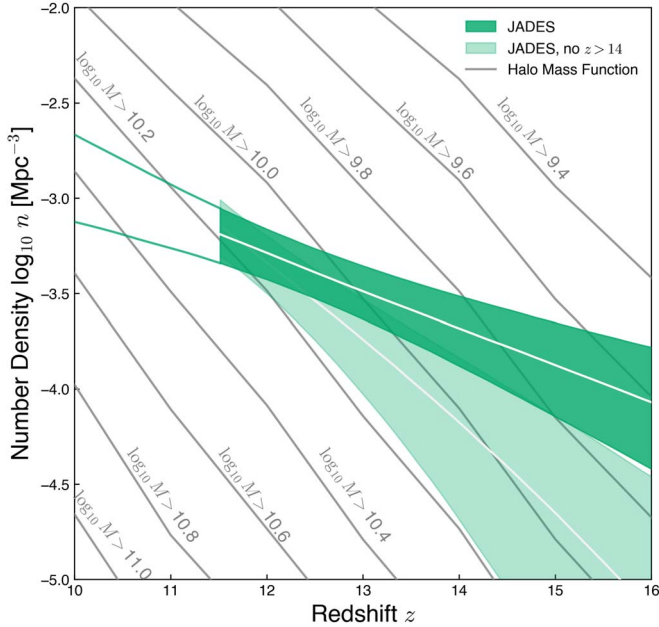


Figure 18. Comparison of the inferred evolution of the JOF galaxy number density $n(z)$ and the abundance of dark matter halos in cosmological simulations. Shown are the inferred number density constraints (dark jade region shows 16%–84% and the white line gives 50%) for models with a linear evolution in $\log_{10} \phi_*$ with redshift z . The grid of gray lines show the abundance of dark matter halos with masses greater than $\log_{10} M \sim 9.4 - 11$ computed from the AbacusSummit simulation suite (Maksimova et al. 2021). In the inferred JOF $n(z)$, if simply matched by abundance the halo mass of the typical galaxy would vary by roughly a factor of ~ 10 . If instead we were to discard the $z > 14$ objects and fit an exponential evolution to $\log_{10} \phi_*$, the typical galaxy would mostly track a halo mass $= \log_{10} M \sim 10$ (light jade region). For reference, we indicate the extrapolation of the inferred number density constraints to lower redshifts with jade lines.

can fit the rest-frame UV photometry with a power law $f_{\nu} \propto \lambda^{2+\beta}$ and jointly constrain M_{UV} and β given the object redshifts. Figure 19 shows the posterior distribution of M_{UV} and β for the candidate galaxies in our Main Sample at $z > 11.5$. The posterior mean and standard deviation for each parameter are reported in Table 8, and for convenience we also report M_{UV} in Table 2. The maximum-likelihood values for the rest-frame spectral slope are $-2 \gtrsim \beta \gtrsim -3$. These values are comparable to the rest-frame spectral properties of high-redshift photometric samples (e.g., Cullen et al. 2023; Topping et al. 2024), although not quite blue enough to suggest completely dust-free objects (e.g., Cullen et al. 2024).

6.2. Morphology and Size

As expected, these galaxies show small angular sizes. As described in Section 2.3.1, we fit single Sérsic profiles to the individual exposures in the F200W and F277W filters, reporting the half-light radii in Table 2. The posterior distributions are often non-Gaussian and asymmetric. Unsurprisingly, most of the objects are small, with half-light radii below 50 mas, except the unusual $z = 14.32$ galaxy NIRCcam ID 183348.

To characterize the limiting angular resolution of our images, we have also fit Sérsic profiles to the exposures (separated by epoch of observation) in the same bands for known brown dwarfs of similar flux levels in the JOF and wider GOODS-S areas (Hainline et al. 2024a). As in our past work (Robertson et al. 2023), we find that brown dwarfs in the JADES Deep imaging are recovered with 95% upper limits on sizes of 20 mas in F200W, so we regard objects with 95% lower limits above 20 mas as inconsistent with a point source. As such, candidates NIRCcam IDs 16699, 160071, and 55733 are

Table 8
Sample Physical Properties, Assuming the Best-fit Redshift

Name	NIRCam ID	z_{phot}	M_{UV}	β	$\log_{10} M_{\star} [M_{\odot}]$	SFR [$M_{\odot} \text{ yr}^{-1}$]
JADES+53.09731-27.84714	74977	11.53	-17.66 ± 0.14	-2.09 ± 0.28	$7.63^{+0.79}_{-0.53}$	$0.47^{+0.47}_{-0.42}$
JADES+53.02618-27.88716	16699	11.56	-17.94 ± 0.15	-2.91 ± 0.35	$7.08^{+0.20}_{-0.27}$	$0.29^{+0.20}_{-0.14}$
JADES+53.04017-27.87603	33309	12.1	-17.73 ± 0.10	-2.46 ± 0.24	$7.62^{+0.21}_{-0.20}$	$0.02^{+0.08}_{-0.02}$
JADES+53.03547-27.90037	160071	12.38	-18.16 ± 0.11	-2.43 ± 0.27	$7.81^{+0.28}_{-0.54}$	$0.20^{+0.52}_{-0.19}$
JADES+53.06475-27.89024	13731	12.93	-18.78 ± 0.04	-2.73 ± 0.13	$7.90^{+0.19}_{-0.20}$	$0.18^{+0.52}_{-0.18}$
JADES+53.02868-27.89301	11457	13.52	-18.55 ± 0.11	-2.46 ± 0.30	$7.08^{+0.13}_{-0.03}$	$1.14^{+1.15}_{-0.13}$
JADES+53.07557-27.87268	376946	14.38	-18.30 ± 0.22	-2.42 ± 0.56	$7.38^{+0.84}_{-0.21}$	$0.96^{+1.23}_{-0.79}$
JADES+53.08294-27.85563	183348	14.39	-20.93 ± 0.04	-2.40 ± 0.12	$8.86^{+0.35}_{-0.03}$	$6.45^{+2.18}_{-4.53}$
JADES+53.10762-27.86013	55733	14.63	-18.54 ± 0.13	-2.52 ± 0.36	$7.80^{+0.58}_{-0.05}$	$0.78^{+0.82}_{-0.66}$

Note. The UV absolute magnitude M_{UV} and rest-frame UV slope β are jointly fit to common PSF Kron photometry for each object. We report here the mean and standard deviation of other posterior distributions for each parameter. The SFRs are averaged over the last 10 Myr of the inferred star formation histories (SFHs).

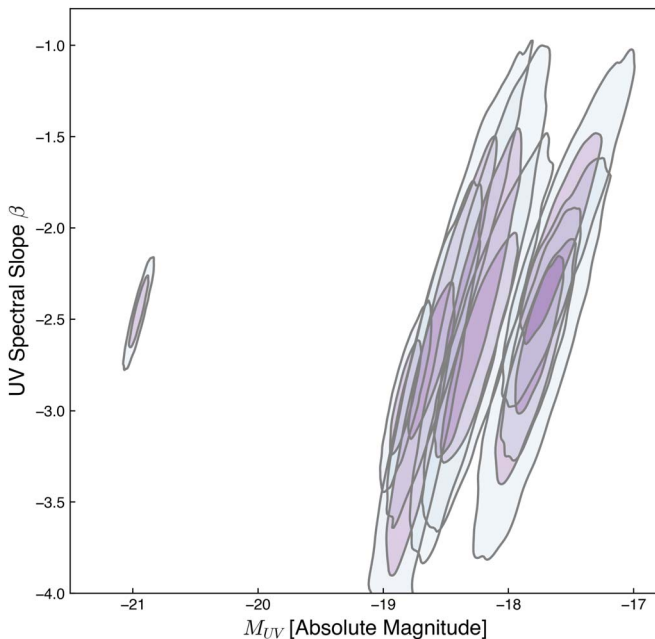


Figure 19. Posterior distributions of rest-frame UV absolute magnitude M_{UV} and spectral slope β for candidate galaxies in our Main Sample at $z > 11.5$. Shown as kernel-density-estimated contours are the 68% and 95% credibility intervals on the joint posterior distributions for each object. The maximum-likelihood values for the UV spectral slope are $-2 \gtrsim \beta \gtrsim -3$. The outlier at $M_{\text{UV}} \approx -21$ is NIRCam ID 183348, spectroscopically confirmed at $z = 14.32$ by S. Carniani et al. (2024, in preparation).

resolved, with half-light angular sizes up to 50 mas and half-light physical sizes of 132, 118, and 142 pc, respectively. The galaxy NIRCam ID 183348 spectroscopically confirmed at $z = 14.32$ by S. Carniani et al. (2024, in preparation) shows a size of 76 mas, or about 240 pc. The remaining sources are consistent with a point source, though many have a nonnegligible probability of having larger sizes. We note that objects NIRCam IDs 13731 and 376946 are both constrained to be very small. In addition to the multiband *Forcepho* fit reported in Table 2, independent single-band *Forcepho* fits to NIRCam ID 13731 infer its size be less than 10 and 16 mas (95th percentile) in F200W and F277W, respectively. While NIRCam ID 376946 appears unresolved in F200W and F277W, it appears more extended in some medium-band filters. Regardless, the sizes of these objects are small enough

that we expect their extents do not impact their detection completeness (e.g., Figure 13).

These results are similar to those found in Robertson et al. (2023), where two of the four $z > 10$ galaxies were resolved. One consequence of being resolved is that the light from these galaxies cannot be purely from an accreting massive black hole (Tacchella et al. 2023). Other spectroscopically confirmed galaxies at $z > 12$ have had size measurements inferred from scene modeling, and show sizes of $R_{1/2} \sim 100\text{--}300$ pc (e.g., Wang et al. 2023). Collectively, these results indicate that compact sizes are a common property of many high-redshift galaxies and candidates.

6.3. Star Formation Rate Histories

To perform detailed modeling of the SEDs in terms of stellar populations, we use the *Prospector* code (Johnson et al. 2021), following the methods described in Tacchella et al. (2022, 2023). Briefly, we assume a variable SFH with a bursty continuity prior, with eight time bins spanning 0–5 Myr, 5–10 Myr, and 6 Myr logarithmically spaced up to $z = 25$. We allow the redshift to vary within the *EAZY* posterior. We adopt a single metallicity for both stars and gas, assuming a truncated lognormal centered on $\log(Z/Z_{\odot}) = -1.5$ with width of 0.5, minimum of -2.0 , and maximum of 0.0. We model dust attenuation using a two-component model with a flexible attenuation curve. For the stellar population synthesis, we adopt the MIST isochrones (Choi et al. 2016) that include effects of stellar rotation but not binaries, and assume a Chabrier (2003) initial mass function between 0.08 and $120 M_{\odot}$. No Ly α emission line is added to the model to account for resonant absorption effects, while the IGM absorption model (Madau 1995; Inoue et al. 2014) is taken into account (normalization is a free parameter). We do not try to constrain independently the effects of possible additional Ly α wing-damping absorption. For consistency with Figures 2–9, we use the $r = 0''.1$ aperture fluxes, but we note that using the $r = 0''.3$ aperture fluxes provide quantitatively similar results for these compact objects. We put an error floor of 5% on the photometry. The rest of the nebular emission (emission lines and continuum) is self-consistently modeled (Byler et al. 2017) with two parameters, the gas-phase metallicity (tied to the stellar metallicity), and the ionization parameter (uniform prior in $-4 < \log(U) < -1$). By combining these inferred stellar population properties with the size measurements from

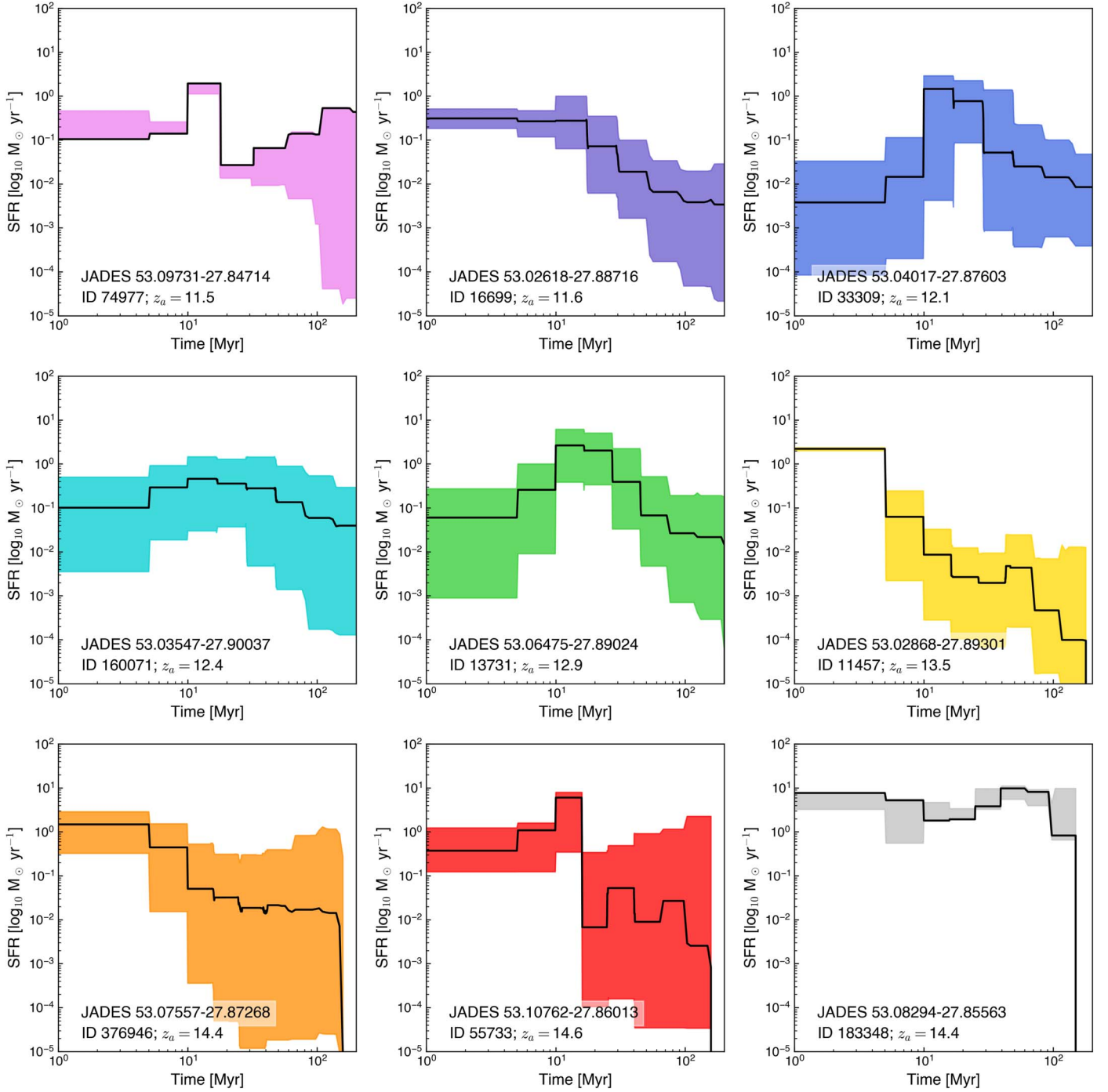


Figure 20. SFHs inferred using the `Prospector` code (Johnson et al. 2021), assuming a continuity prior and following the methods described in Tacchella et al. (2023). The galaxy candidates show SFRs $\approx 0.1\text{--}1 M_{\odot} \text{ yr}^{-1}$ over the last ~ 10 Myr, measured backward from the epoch of observation. Roughly half of the objects show increasing SFHs, while the others indicate a peak or burst in their SFRs roughly 10 Myr before the observation epoch. This feature may indicate an episode of miniquenching (Looser et al. 2023) in these objects. Only one galaxy indicates a comparable or higher SFR $t \sim 100$ Myr before the observation epoch, such that no object indicates evidence of substantial star formation before $z \sim 15$. Each galaxy is labeled by both their [R.A., decl.] designation, photometric redshift, and internal JADES NIRCam ID.

Forcepho, we can additionally infer the stellar mass and SFR surface densities of the candidate galaxies.

Figure 20 shows the resulting SFHs of the eight galaxy candidates in our sample. The average SFR over the last 10 Myr is also reported for each candidate galaxy in Table 8. In each case, the continuity prior on the SFH was used to inform the point-to-point SFR variations in the galaxies. For each object, the photometry listed in Tables 3–5 were used, except

for the faintest object NIRcam ID 74977 ($f_{\nu} \sim 2\text{--}3$ nJy) where the lower SNR Kron fluxes were used. We find that the typical SFRs of these objects are $\text{SFR} \approx 0.1\text{--}10 M_{\odot} \text{ yr}^{-1}$ over the last $t \sim 10\text{--}30$ Myr. The galaxies formed substantial fractions of their stars in the recent past, and have characteristic ages of just a few tens of millions of years. A few of the objects (NIRCam IDs 13731, 33309, 55733, and 74977) show features in their SFHs roughly 10–20 Myr before their observed epoch, with a

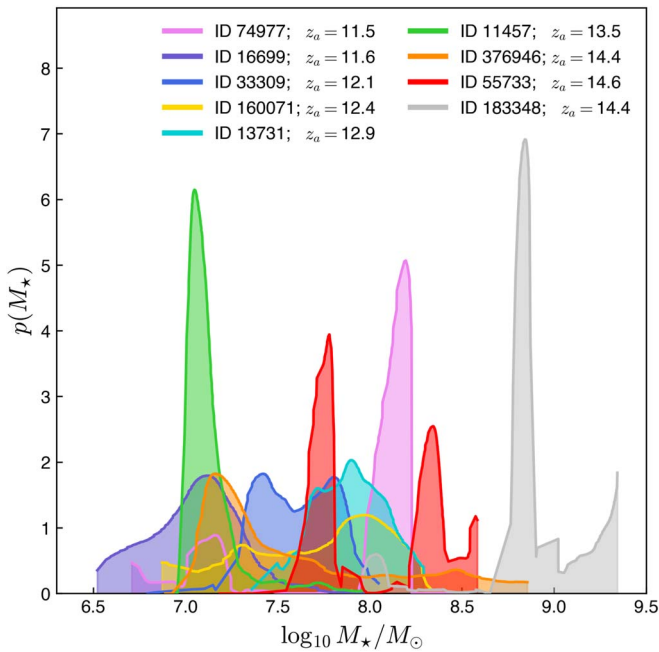


Figure 21. Posterior distribution of stellar mass for candidate $z > 11.5$ galaxies. Shown are the stellar mass distributions constructed from posterior samples of the `Prospector` code (Johnson et al. 2021). The objects have inferred stellar masses of $M_* \sim 10^7\text{--}10^8 M_\odot$, comparable to those inferred for the spectroscopically confirmed $z \sim 12\text{--}13$ galaxies analyzed by Robertson et al. (2023). Each galaxy candidate is labeled by its JADES NIRCam ID and photometric redshift, and color coded the same in Figure 20.

flat or even falling SFR thereafter. We speculate that these features may reflect “miniquenching” events where star formation shuts down briefly after exhausting or removing fuel (Looser et al. 2023). For the other objects, the SFHs appear to increase to the epoch of observation, suggesting some upswing in the SFRs and luminosities of these objects. In two cases (NIRCam IDs 74977 and 183348) the objects show evidence of comparable or higher SFRs 100 Myr before the observed epoch. For NIRCam ID 74977, this early star formation would correspond to $z \sim 14.2$. For NIRCam ID 183348, the early star formation would potentially start at $z \sim 20$. The uncertainties on the SFHs are large, and we cannot constrain well the SFR before $z \sim 15$ for most objects. Given the physical sizes of the objects of $R_{1/2} \approx 50\text{--}200$ pc inferred from the `Forcepho` analysis, the SFR surface densities of these objects are $\Sigma_{\text{SFR}} \sim 10\text{--}100 M_\odot \text{ yr}^{-1} \text{ kpc}^2$. Both the SFRs and SFR surface densities are comparable to those found by Robertson et al. (2023) for spectroscopically confirmed galaxies at $z \sim 12\text{--}13$, and consistent with being from the same galaxy population.

The above analysis assumes no luminous contribution from an active galactic nucleus (AGN). Of course, some of these galaxies may possibly host a luminous AGN, as have been found or suspected in some other high-redshift galaxies (e.g., Maiolino et al. 2023a, 2024; Übler et al. 2023; Goulding et al. 2023; Kokorev et al. 2023). AGN emission would decrease the inferred stellar emission and require a reassessment of the SFHs and stellar masses, and possibly the photometric redshifts. We note that the fact that some of these galaxies are angularly resolved implies that some of the emission is stellar.

6.4. Stellar Mass Distributions

Figure 21 presents the marginal stellar mass distributions inferred from `Prospector` fits to the observed photometry. The posterior samples of the galaxy properties were used to produce marginal distributions of the stellar mass, following the procedure described in Robertson et al. (2023). In agreement with Robertson et al. (2023), we find that the stellar masses of these $z \sim 12\text{--}15$ galaxies are $M_* \sim 10^7\text{--}10^9 M_\odot$. Given the sizes of $R_{1/2} \sim 50\text{--}200$ pc we measure from the surface brightness profiles, the stellar mass surface densities of the objects are then $\Sigma_* \sim 10^3\text{--}10^4 M_\odot \text{ pc}^{-2}$. For a self-gravitating system, the dynamical timescale is then comparable to the star formation timescale inferred in Section 6.3. Overall, in agreement with our previous findings in Robertson et al. (2023), these objects are consistent with rapidly star-forming, compact galaxies with formation timescales comparable to a few dynamical times. Using the simple abundance matching comparison with dark matter halos discussed in Section 5.5, we note that matching to number densities would place these objects in $M_h \sim 10^{10} M_\odot$ dark matter halos, with $M_*/M_h \sim 10^{-1}\text{--}10^{-3}$, well above the present-day stellar mass to halo mass relations (e.g., Wechsler & Tinker 2018).

7. Discussion

The luminosity function evolution remains the best current indicator of the connection between galaxies, dark matter halos, and cosmic reionization at the highest redshifts (for a review, see Robertson 2022). These results from the JOF provide some new insight into the process of high-redshift galaxy formation.

The JOF provides the best currently available data for probing faint galaxies at redshifts $z > 12$, given its depth and filter array. Using an area twice the size of the Hubble UDF, the JOF area reaches a deeper limit (30.2–30.5 AB) and has 14 JWST filters including the ultradeep JADES Program 1210. The inclusion of deep F162M provides an essential check on the reality of the highest-redshift candidates.

Of our Main Sample, none of the galaxies are brighter than $M_{\text{UV}} = -18.6$, and many have $M_{\text{UV}} > -18$. The depth allows us to constrain the UV luminosity function to fainter limits at $z \sim 14$ than previously possible, while retaining tighter control of systematics by having additional medium-band filters to probe the Lyman break with more fidelity. Following the stellar population modeling procedure of Tacchella et al. (2023), we find that the SFRs and stellar mass properties are comparable to galaxies spectroscopically confirmed at $z \sim 12\text{--}13$ (Wang et al. 2023; Curtis-Lake et al. 2023; Robertson et al. 2023). Using the `Forcepho` forward model for the surface brightness distribution of these galaxies, we find that they have compact sizes of $R_{1/2} \sim 50\text{--}200$ pc, also in agreement with spectroscopically confirmed galaxies at these redshifts (Wang et al. 2023; Robertson et al. 2023).

In agreement with previous determinations of the UV luminosity function in extragalactic JWST fields (Pérez-González et al. 2023a; Donnan et al. 2023b; Harikane et al. 2023, 2024; Adams et al. 2024; Finkelstein et al. 2024; McLeod et al. 2024; Willott et al. 2024), we find that the luminosity function of galaxies has smoothly declined from $z \sim 8$, as first established by HST observations (e.g., McLure et al. 2013), to $z \sim 12$. Our results for the abundance of galaxies at $z \sim 12$ are in broad agreement with the literature values, as

shown in Figures 16 and 17. We do note that our inferred UV luminosity density at $z \sim 14$ is lower than that reported by Finkelstein et al. (2024), but the uncertainties are large.

However, our selection completeness using the JOF observations is sensitive to galaxies out to $z \sim 20$ when the Ly α break enters F250M. With a suitable revision to our selection, we would be sensitive to bright galaxies at even greater distances. Our work presents a new method for modeling the redshift-dependent UV luminosity function incorporating both detections and nondetections to constrain its evolution over the redshift range $z \approx 11\text{--}20$ where our completeness is high. From the lack of galaxy candidates at $z > 15$, we find that the decline to $z > 14$ continues at $d \log \phi_*/dz \sim -0.2$ with our nominal Main Sample presented in Tables 2–5. We note that uncertainties owing to cosmic variance are clearly nonnegligible for the JOF, and a larger sample of galaxies at $z > 11.5$ is needed to confirm this decline. Nonetheless, we now know that the $M_{UV} \sim -21$ object NIRCam ID 183348 selected by our JOF medium-band photometry to be at a photometric redshift of $z \approx 14.4$ has been spectroscopically confirmed at $z = 14.32$ by S. Carniani et al. (2024, in preparation). As Figure 18 shows, the evolving luminosity density at $z > 14$ we infer from NIRCam ID 183348 and our photometric candidates, while declining, still requires a constant remapping between galaxy and halo abundance, with increasing efficiency in low-mass halos at higher redshifts. This evolution is in contrast to the possibility that $z > 14$ galaxies were not abundant, where a rapid drop in the UV luminosity density would track more closely the abundance of $M_{vir} \sim 10^{10} M_\odot$ halos and the galaxy efficiency could stabilize at early times. Given the confirmation of NIRCam ID 183348, we see no evidence for such a stabilization in the efficiency of galaxy formation out to $z \sim 14$ or beyond.

Lastly, since our results are consistent with prior literature results at $z \sim 12$, theoretical models that match those observations also match ours. For instance, the feedback-free models of Dekel et al. (2023) and Li et al. (2023) agree with our $z \sim 12$ observations for an efficiency of $\epsilon_{max} \approx 0.2$. Models for the evolving number counts of high-redshift galaxies based on dust-free populations (e.g., Ferrara et al. 2023) also predict an SFR density evolution to $z \sim 15$ in agreement with our inferences, assuming all our candidates are really high-redshift sources (Ferrara 2024).

8. Summary and Conclusions

Using ultra-deep JWST observations of the JOF, we search for the most distant galaxies in the Universe. With 14 JWST and up to nine HST filters covering the JOF, we can carefully select galaxies at $z > 12$ by identifying dropouts in NIRCam F162M and bluer filters using SED template-based photometric redshift fitting. Our findings include:

1. We select nine galaxy candidates at $z \sim 12\text{--}15$ and no galaxy candidates at $z \gtrsim 15$. These objects include the most distant candidates detected in more than five filters and displaying a dropout in more than 10 filters. Our sample selection includes a galaxy at $z = 14.32$ since spectroscopically confirmed. Simulations of our detection and photometry methods and our prior spectroscopic confirmations of high-redshift JADES sources suggest that the other candidates without spectroscopic confirmation are robust. Several of our candidates have been

identified in previous analyses, including Hainline et al. (2024b) and Williams et al. (2024).

2. These objects show apparent total magnitudes of $m_{AB} \sim 29.5\text{--}30.5$ in the rest-frame UV and blue rest-UV spectral slopes $-2 \gtrsim \beta \gtrsim -3$.
3. Performing detailed structural modeling with `Forcepho` and stellar population inference using `Prospector`, we find that the galaxies have SFRs $\approx 0.1\text{--}10 M_\odot \text{ yr}^{-1}$, stellar masses of $M_* \sim 10^7\text{--}10^9 M_\odot$, sizes of $R \sim 50\text{--}200$ pc, and stellar ages of $t_* \approx 30\text{--}50$ Myr. The properties of our low-mass candidates are comparable to the properties of $z \sim 12\text{--}13$ galaxies with confirmed redshifts, as first identified by the JADES collaboration.
4. We develop a new forward-modeling method to infer constraints on the evolving UV luminosity function without binning in redshift or luminosity while marginalizing over the photometric redshift posterior distributions of the candidates in our sample. This method allows for an accounting of potential contamination by adjacent redshifts and includes the impact of nondetections on the inferred galaxy luminosity function evolution.
5. With the population of $z > 12$ galaxy candidates newly discovered in the JOF, we provide an inference on the $z \sim 15$ luminosity function and a refined measure of the luminosity function at $z \sim 12$ in agreement with literature values. At $z \sim 15$, we infer a continued decline from $z \sim 12$. Over the redshift range $z \sim 12\text{--}14$, where we have detected galaxies, we infer a factor of 2.5 decline in the luminosity function normalization ϕ_* and a corresponding decline in the luminosity density ρ_{UV} . We note that cosmic variance uncertainties for the high-redshift JOF sample are not negligible, and this decline should be confirmed with a larger sample over a wider area.

This demonstrates the immediate impact new JWST observations can have on our knowledge of the distant Universe. With high-redshift galaxy populations now established fewer than 300 million years after the Big Bang, we have extended our reach into the cosmic past by 40% during the first 18 months of JWST operations.

Acknowledgments

The JADES Collaboration thanks the Instrument Development Teams and the instrument teams at the European Space Agency and the Space Telescope Science Institute for the support that made this program possible. The authors acknowledge use of the lux supercomputer at UC Santa Cruz, funded by NSF MRI grant AST 1828315.

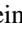




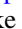






B.E.R., B.D.J., D.J.E., P.A.C., E.E., M.R., F.S., and C.N.A.W. acknowledge support from the JWST/NIRCam contract to the University of Arizona, NAS5-02015. B.E.R. acknowledges support from JWST Program 3215. D.J.E. is supported as a Simons Investigator. S.A. acknowledges support from grant PID2021-127718NB-I00 funded by the Spanish Ministry of Science and Innovation/State Agency of Research (MICIN/AEI/ 10.13039/501100011033). W.B., F.D.E., R.M., and J.W. acknowledge support by the Science and Technology Facilities Council (STFC), ERC Advanced Grant 695671 “QUENCH.” A. J.B., J.C., and G.C.J. acknowledge funding from the “First-Galaxies” Advanced Grant from the European Research Council (ERC) under the European Unions Horizon 2020 research and innovation program (grant agreement No. 789056).






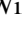



S.C. acknowledges support by European Unions HE ERC Starting Grant No. 101040227—WINGS. E.C.L. acknowledges support of an STFC Webb Fellowship (ST/W001438/1). F.D.E., R.M., and J.W. acknowledge support by UKRI Frontier Research grant RISEandFALL. Funding for this research was provided by the Johns Hopkins University, Institute for Data Intensive Engineering and Science (IDIES). R.M. also acknowledges funding from a research professorship from the Royal Society. The Cosmic Dawn Center (DAWN) is funded by the Danish National Research Foundation under grant DNRF140. P.G.P.-G. acknowledges support from grant PID2022-139567NB-I00 funded by Spanish Ministerio de Ciencia e Innovación MCIN/AEI/10.13039/501100011033, FEDER, UE. D.P. acknowledges support by the Huo Family Foundation through a P.C. Ho PhD Studentship. R.S. acknowledges support from an STFC Ernest Rutherford Fellowship (ST/S004831/1). H.Ü. gratefully acknowledges support by the Isaac Newton Trust and by the Kavli Foundation through a Newton-Kavli Junior Fellowship. L.W. acknowledges support from the National Science Foundation Graduate Research Fellowship under grant No. DGE-2137419. The research of C. C.W. is supported by NOIRLab, which is managed by the Association of Universities for Research in Astronomy (AURA) under a cooperative agreement with the National Science Foundation.

Facility: HST (ACS, WFC3) and JWST(NIRCam).

Software: astropy (Astropy Collaboration et al. 2018, 2022), EAZY (Brammer et al. 2008), Source Extractor (Bertin & Arnouts 1996), photutils (Bradley et al. 2023), and nautilus (Lange 2023).

ORCID iDs

Brant Robertson  <https://orcid.org/0000-0002-4271-0364>
 Benjamin D. Johnson  <https://orcid.org/0000-0002-9280-7594>
 Sandro Tacchella  <https://orcid.org/0000-0002-8224-4505>
 Daniel J. Eisenstein  <https://orcid.org/0000-0002-2929-3121>
 Kevin Hainline  <https://orcid.org/0000-0003-4565-8239>
 Santiago Arribas  <https://orcid.org/0000-0001-7997-1640>
 William M. Baker  <https://orcid.org/0000-0003-0215-1104>
 Andrew J. Bunker  <https://orcid.org/0000-0002-8651-9879>
 Stefano Carniani  <https://orcid.org/0000-0002-6719-380X>
 Phillip A. Cargile  <https://orcid.org/0000-0002-1617-8917>
 Courtney Carreira  <https://orcid.org/0000-0001-6301-3667>
 Stephane Charlot  <https://orcid.org/0000-0003-3458-2275>
 Jacopo Chevallard  <https://orcid.org/0000-0002-7636-0534>
 Mirko Curti  <https://orcid.org/0000-0002-2678-2560>
 Emma Curtis-Lake  <https://orcid.org/0000-0002-9551-0534>
 Francesco D'Eugenio  <https://orcid.org/0000-0003-2388-8172>
 Eiichi Egami  <https://orcid.org/0000-0003-1344-9475>
 Ryan Hausen  <https://orcid.org/0000-0002-8543-761X>
 Jakob M. Helton  <https://orcid.org/0000-0003-4337-6211>
 Peter Jakobsen  <https://orcid.org/0000-0002-6780-2441>
 Zhiyuan Ji  <https://orcid.org/0000-0001-7673-2257>
 Gareth C. Jones  <https://orcid.org/0000-0002-0267-9024>
 Roberto Maiolino  <https://orcid.org/0000-0002-4985-3819>
 Michael V. Maseda  <https://orcid.org/0000-0003-0695-4414>
 Erica Nelson  <https://orcid.org/0000-0002-7524-374X>
 Pablo G. Pérez-González  <https://orcid.org/0000-0003-4528-5639>
 Dávid Puskás  <https://orcid.org/0000-0001-8630-2031>

Marcia Rieke  <https://orcid.org/0000-0002-7893-6170>
 Renske Smit  <https://orcid.org/0000-0001-8034-7802>
 Fengwu Sun  <https://orcid.org/0000-0002-4622-6617>
 Hannah Übler  <https://orcid.org/0000-0003-4891-0794>
 Lily Whitler  <https://orcid.org/0000-0003-1432-7744>
 Christina C. Williams  <https://orcid.org/0000-0003-2919-7495>
 Christopher N. A. Willmer  <https://orcid.org/0000-0001-9262-9997>
 Chris Willott  <https://orcid.org/0000-0002-4201-7367>
 Joris Witstok  <https://orcid.org/0000-0002-7595-121X>

References

- Adams, N. J., Conselice, C. J., Ferreira, L., et al. 2023, *MNRAS*, 518, 4755
 Adams, N. J., Conselice, C. J., Austin, D., et al. 2024, *ApJ*, 965, 169
 Akhlaghi, M. 2019, arXiv:1909.11230
 Akhlaghi, M., & Ichikawa, T. 2015, *ApJS*, 220, 1
 Arrabal Haro, P., Dickinson, M., Finkelstein, S. L., et al. 2023, *ApJL*, 951, L22
 Astropy Collaboration, Price-Whelan, A. M., Lim, P. L., et al. 2022, *ApJ*, 935, 167
 Astropy Collaboration, Price-Whelan, A. M., Sipőcz, B. M., et al. 2018, *AJ*, 156, 123
 Atek, H., Shuntov, M., Furtak, L. J., et al. 2023, *MNRAS*, 519, 1201
 Bagley, M. B., Finkelstein, S. L., Koekemoer, A. M., et al. 2023a, *ApJL*, 946, L12
 Bagley, M. B., Pirzkal, N., Finkelstein, S. L., et al. 2024, *ApJL*, 965, L6
 Baker, W. M., Tacchella, S., Johnson, B. D., et al. 2023, arXiv:2306.02472
 Bertin, E., & Arnouts, S. 1996, *A&AS*, 117, 393
 Bouwens, R., Illingworth, G., Oesch, P., et al. 2023, *MNRAS*, 523, 1009
 Bouwens, R. J., Smit, R., Schouws, S., et al. 2022, *ApJ*, 931, 160
 Bradley, L., Sipőcz, B., & Robitaille, T. 2023, astropy/photutils: 1.9.0, 1.9.0, Zenodo, doi:10.5281/zenodo.8248020
 Brammer, G. B., van Dokkum, P. G., & Coppi, P. 2008, *ApJ*, 686, 1503
 Bunker, A. J., Cameron, A. J., Curtis-Lake, E., et al. 2023, arXiv:2306.02467
 Byler, N., Dalcanton, J. J., Conroy, C., & Johnson, B. D. 2017, *ApJ*, 840, 44
 Carnall, A. C., McLure, R. J., Dunlop, J. S., & Davé, R. 2018, *MNRAS*, 480, 4379
 Castellano, M., Fontana, A., Treu, T., et al. 2022, *ApJL*, 938, L15
 Chabrier, G. 2003, *PASP*, 115, 763
 Choi, J., Dotter, A., Conroy, C., et al. 2016, *ApJ*, 823, 102
 Cullen, F., McLeod, D. J., McLure, R. J., et al. 2024, *MNRAS*, 531, 997
 Cullen, F., McLure, R. J., McLeod, D. J., et al. 2023, *MNRAS*, 520, 14
 Curtis-Lake, E., Carniani, S., Cameron, A., et al. 2023, *NatAs*, 7, 622
 Dekel, A., Sarkar, K. C., Birnboim, Y., Mandelker, N., & Li, Z. 2023, *MNRAS*, 523, 3201
 D'Eugenio, F., Maiolino, R., Carniani, S., et al. 2023, arXiv:2311.09908
 Donnan, C. T., McLeod, D. J., Dunlop, J. S., et al. 2023b, *MNRAS*, 518, 6011
 Donnan, C. T., McLeod, D. J., McLure, R. J., et al. 2023a, *MNRAS*, 520, 4554
 Eisenstein, D. J., Johnson, B. D., Robertson, B., et al. 2023b, arXiv:2310.12340
 Eisenstein, D. J., Willott, C., Alberts, S., et al. 2023a, arXiv:2306.02465
 Ferrami, G., & Wyithe, J. S. B. 2023, *MNRAS*, 523, L21
 Ferrara, A. 2024, *A&A*, 684, A207
 Ferrara, A., Pallottini, A., & Dayal, P. 2023, *MNRAS*, 522, 3986
 Finkelstein, S. L., Bagley, M. B., Ferguson, H. C., et al. 2023, *ApJL*, 946, L13
 Finkelstein, S. L., Leung, G. C. K., Bagley, M. B., et al. 2024, *ApJL*, 969, L2
 Fujimoto, S., Arrabal Haro, P., Dickinson, M., et al. 2023, *ApJL*, 949, L25
 Gaia Collaboration, Brown, A. G. A., Vallenari, A., et al. 2018, *A&A*, 616, A1
 Garrison, L. H., Eisenstein, D. J., Ferrer, D., Maksimova, N. A., & Pinto, P. A. 2021, *MNRAS*, 508, 575
 Giavalisco, M., Ferguson, H. C., Koekemoer, A. M., et al. 2004, *ApJL*, 600, L93
 Goulding, A. D., Greene, J. E., Setton, D. J., et al. 2023, *ApJL*, 955, L24
 Grogin, N. A., Kocevski, D. D., Faber, S. M., et al. 2011, *ApJS*, 197, 35
 Guhathakurta, P., Tyson, J. A., & Majewski, S. R. 1990, *ApJL*, 357, L9
 Hadzhiyska, B., Tacchella, S., Bose, S., & Eisenstein, D. J. 2021, *MNRAS*, 502, 3599
 Hainline, K. N., Helton, J. M., Johnson, B. D., et al. 2024a, *ApJ*, 964, 66
 Hainline, K. N., Johnson, B. D., Robertson, B., et al. 2024b, *ApJ*, 964, 71
 Harikane, Y., Nakajima, K., Ouchi, M., et al. 2024, *ApJ*, 960, 56
 Harikane, Y., Ouchi, M., Oguri, M., et al. 2023, *ApJS*, 265, 5
 Heintz, K. E., Watson, D., Brammer, G., et al. 2024, *Sci*, 384, 890
 Illingworth, G., Magee, D., Bouwens, R., et al. 2016, arXiv:1606.00841

- Inoue, A. K., Shimizu, I., Iwata, I., & Tanaka, M. 2014, *MNRAS*, **442**, 1805
- Ishigaki, M., Kawamata, R., Ouchi, M., et al. 2018, *ApJ*, **854**, 73
- Ji, Z., Williams, C. C., Tacchella, S., et al. 2023, arXiv:2305.18518
- Johnson, B. D., Leja, J., Conroy, C., & Speagle, J. S. 2021, *ApJS*, **254**, 22
- Koekemoer, A. M., Faber, S. M., Ferguson, H. C., et al. 2011, *ApJS*, **197**, 36
- Kokorev, V., Fujimoto, S., Labbe, I., et al. 2023, *ApJL*, **957**, L7
- Kron, R. G. 1980, *ApJS*, **43**, 305
- Lange, J. U. 2023, *MNRAS*, **525**, 3181
- Leja, J., Speagle, J. S., Johnson, B. D., et al. 2020, *ApJ*, **893**, 111
- Leung, G. C. K., Bagley, M. B., Finkelstein, S. L., et al. 2023, *ApJL*, **954**, L46
- Li, Z., Dekel, A., Sarkar, K. C., et al. 2023, 14662, arXiv:2311.14662
- Looser, T. J., D'Eugenio, F., Maiolino, R., et al. 2023, arXiv:2306.02470
- Lovell, C. C., Harrison, I., Harikane, Y., Tacchella, S., & Wilkins, S. M. 2023, *MNRAS*, **518**, 2511
- Madau, P. 1995, *ApJ*, **441**, 18
- Madau, P., & Dickinson, M. 2014, *ARA&A*, **52**, 415
- Maiolino, R., Scholtz, J., Curtis-Lake, E., et al. 2023a, arXiv:2308.01230
- Maiolino, R., Scholtz, J., Witsstok, J., et al. 2024, *Natur*, **627**, 59
- Maksimova, N. A., Garrison, L. H., Eisenstein, D. J., et al. 2021, *MNRAS*, **508**, 4017
- Mason, C. A., Trenti, M., & Treu, T. 2023, *MNRAS*, **521**, 497
- Mason, C. A., Treu, T., Schmidt, K. B., et al. 2015, *ApJ*, **805**, 79
- McLeod, D. J., Donnan, C. T., McLure, R. J., et al. 2024, *MNRAS*, **527**, 5004
- McLure, R. J., Dunlop, J. S., Bowler, R. A. A., et al. 2013, *MNRAS*, **432**, 2696
- Morishita, T., & Stiavelli, M. 2023, *ApJL*, **946**, L35
- Naidu, R. P., Oesch, P. A., Setton, D. J., et al. 2022b, arXiv:2208.02794
- Naidu, R. P., Oesch, P. A., van Dokkum, P., et al. 2022a, *ApJL*, **940**, L14
- Oke, J. B., & Gunn, J. E. 1983, *ApJ*, **266**, 713
- Pan, Y., & Kravtsov, A. 2023, arXiv:2310.08636
- Pérez-González, P. G., Barro, G., Annunziatella, M., et al. 2023b, *ApJL*, **946**, L16
- Pérez-González, P. G., Costantin, L., Langeroodi, D., et al. 2023a, *ApJL*, **951**, L1
- Rieke, M. J., Robertson, B., Tacchella, S., et al. 2023, *ApJS*, **269**, 16
- Rigby, J., Perrin, M., McElwain, M., et al. 2023, *PASP*, **135**, 048001
- Robertson, B. E. 2022, *ARA&A*, **60**, 121
- Robertson, B. E., Tacchella, S., Johnson, B. D., et al. 2023, *NatAs*, **7**, 611
- Rowe, B. T. P., Jarvis, M., Mandelbaum, R., et al. 2015, *A&C*, **10**, 121
- Schechter, P. 1976, *ApJ*, **203**, 297
- Sérsic, J. L. 1968, Atlas de Galaxias Australes (Cordoba: Observatorio Astronomico)
- Shen, X., Borrow, J., Vogelsberger, M., et al. 2024, *MNRAS*, **527**, 2835
- Shen, X., Vogelsberger, M., Boylan-Kolchin, M., Tacchella, S., & Kannan, R. 2023a, *MNRAS*, **525**, 3254
- Steidel, C. C., Pettini, M., & Hamilton, D. 1995, *AJ*, **110**, 2519
- Sun, G., Faucher-Giguère, C.-A., Hayward, C. C., et al. 2023, *ApJL*, **955**, L35
- Tacchella, S., Eisenstein, D. J., Hainline, K., et al. 2023, *ApJ*, **952**, 74
- Tacchella, S., Finkelstein, S. L., Bagley, M., et al. 2022, *ApJ*, **927**, 170
- Topping, M. W., Stark, D. P., Endsley, R., et al. 2024, *MNRAS*, **529**, 4087
- Treu, T., Calabrò, A., Castellano, M., et al. 2023, *ApJL*, **942**, L28
- Übler, H., Maiolino, R., Curtis-Lake, E., et al. 2023, *A&A*, **677**, A145
- Wang, B., Fujimoto, S., Labbé, I., et al. 2023, *ApJL*, **957**, L34
- Wechsler, R. H., & Tinker, J. L. 2018, *ARA&A*, **56**, 435
- Williams, C. C., Albers, S., Ji, Z., et al. 2024, *ApJ*, **968**, 34
- Willott, C. J., Desprez, G., Asada, Y., et al. 2024, *ApJ*, **966**, 74
- Wyithe, J. S. B., Yan, H., Windhorst, R. A., & Mao, S. 2011, *Natur*, **469**, 181
- Yung, L. Y. A., Somerville, R. S., Finkelstein, S. L., Wilkins, S. M., & Gardner, J. P. 2024, *MNRAS*, **527**, 5929
- Zavala, J. A., Buat, V., Casey, C. M., et al. 2023, *ApJL*, **943**, L9